University of Montana

ScholarWorks at University of Montana

Numerical Terradynamic Simulation Group Publications

Numerical Terradynamic Simulation Group

9-2009

Satellite assessment of land surface evapotranspiration for the pan-Arctic domain

Qiaozhen Mu

Lucas A. Jones

John S. Kimball
University of Montana - Missoula

Kyle C. McDonald
City College of New York

Steven W. Running
University of Montana - Missoula

Follow this and additional works at: https://scholarworks.umt.edu/ntsg_pubs

Let us know how access to this document benefits you.

Recommended Citation

Mu, Q., L. A. Jones, J. S. Kimball, K. C. McDonald, and S. W. Running (2009), Satellite assessment of land surface evapotranspiration for the pan-Arctic domain, Water Resour. Res., 45, W09420, doi:10.1029/2008WR007189

Satellite assessment of land surface evapotranspiration for the pan-Arctic domain

Qiaozhen Mu,[1] Lucas A. Jones,[1] John S. Kimball,[2] Kyle C. McDonald,[3] and Steven W. Running[1]

[1] Regional evapotranspiration (ET), including water loss from plant transpiration and soil evaporation, is essential to understanding interactions between land-atmosphere surface energy and water balances. Vapor pressure deficit (VPD) and surface air temperature are key variables for stomatal conductance and ET estimation. We developed an algorithm to estimate ET using the Penman-Monteith approach driven by Moderate Resolution Imaging Spectroradiometer (MODIS)-derived vegetation data and daily surface meteorological inputs including incoming solar radiation, air temperature, and VPD. The model was applied using alternate daily meteorological inputs, including (1) site level weather station observations, (2) VPD and air temperature derived from the Advanced Microwave Scanning Radiometer (AMSR-E) on the EOS Aqua satellite, and (3) Global Modeling and Assimilation Office (GMAO) reanalysis meteorology-based surface air temperature, humidity, and solar radiation data. Model performance was assessed across a North American latitudinal transect of six eddy covariance flux towers representing northern temperate grassland, boreal forest, and tundra biomes. Model results derived from the three meteorology data sets agree well with observed tower fluxes ($r > 0.7$; $P < 0.003$; root mean square error of latent heat flux <30 W m^{-2}) and capture spatial patterns and seasonal variability in ET. The MODIS-AMSR-E−derived ET results also show similar accuracy to ET results derived from GMAO, while ET estimation error was generally more a function of algorithm parameterization than differences in meteorology drivers. Our results indicate significant potential for regional mapping and monitoring daily land surface ET using synergistic information from satellite optical IR and microwave remote sensing.

1. Introduction

[2] The terrestrial water cycle is of critical importance to a wide array of Earth system processes. It plays a central role in climate and meteorology, plant community dynamics, carbon and nutrient biogeochemistry [*Vörösmarty et al.*, 1998]. Evapotranspiration (ET) is an important component of the terrestrial water cycle. At the global scale it represents more than 60% of precipitation inputs [*Korzoun et al.*, 1978; *L'vovich and White*, 1990] and thereby conveys an important constraint on water availability at the land surface. Over a relatively long time period (i.e., a season or a year), the available water for humans and ecosystems in a given region can be approximated by the difference between accumulated precipitation and ET [*Donohue et al.*, 2007]. With increasing human population and rapid climate change, fresh water availability on land has become critically important both for the environment and society. Through links between stomatal conductance, carbon exchange, and water use efficiency in plant canopies [e.g., *Hari et al.*, 1986; *Raich et al.*, 1991; *Woodward and Smith*, 1994; *Sellers et al.*, 1996; *Farquhar et al.*, 2002], ET serves as a regulator of key ecosystem processes. This, in turn, controls the large areal distribution of plant communities and vegetation net primary production [e.g., *Prentice et al.*, 1992; *Neilson*, 1995; *Woodward et al.*, 1995; *Marsden et al.*, 1996; *Dang et al.*, 1997; *Oren et al.*, 1999; *Misson et al.*, 2004].

[3] Boreal forest and Arctic tundra in the pan-Arctic basin and Alaska cover approximately 25 million km^2 of the northern high latitudes ($>50°$N) and 30% of the combined North American and Eurasian land mass [*Kimball et al.*, 2006]. The ecosystems in this pan-Arctic domain are important contributors to the net balance of water, energy and carbon exchange between the atmosphere and the biosphere [*McGuire et al.*, 2008].

[4] A large number of physical factors are involved in soil evaporation and plant transpiration processes, including microclimate, plant biophysics and landscape heterogeneity, making accurate assessment of ET a challenge [*Gash*, 1987; *Friedl*, 1996; *Maddock et al.*, 1998; *Janowiak et al.*, 1998;

---

[1]Numerical Terradynamic Simulation Group, College of Forestry and Conservation, University of Montana, Missoula, Montana, USA.
[2]Flathead Lake Biological Station, Polson, Montana, USA.
[3]NASA Jet Propulsion Laboratory, Pasadena, California, USA.

Vörösmarty et al., 1998; *McVicar et al.*, 2007]. Remotely sensed data, especially those from polar-orbiting satellites, provide temporally and spatially continuous information at high latitudes over vegetated surfaces useful for regional measurement and monitoring of surface biophysical variables affecting ET, including albedo, biome type and leaf area index (LAI) [*Los et al.*, 2000]. The Moderate Resolution Imaging Spectroradiometer (MODIS) onboard NASA's Terra and Aqua satellites, provide unprecedented information regarding vegetation and surface energy [*Justice et al.*, 2002], which can be used for regional- and global-scale ET estimation in near real time. *Mu et al.* [2007b] modified a remote sensing ET algorithm (RS-ET) proposed by *Cleugh et al.* [2007] that calculates ET using the Penman-Monteith (P-M) equation with daily meteorological inputs and sensed leaf area index data from MODIS to estimate the surface conductance of the P-M equation. The RS-ET algorithm employs reanalysis surface meteorological data from NASA's Global Modeling and Assimilation Office (GMAO, v. 4.0.0) for regional estimation and mapping of ET globally. However, reanalysis meteorological products have been found to exhibit significant bias in high-latitude locations due to sparse meteorological observations and complex land surface feedback processes [*Zhao et al.*, 2006; *Zhang et al.*, 2007]. Error in driving meteorology can represent a significant proportion of overall error in high-level remote sensing products [*Heinsch et al.*, 2006].

[5] Previous satellite-based surface energy balance models (SEBS) [*Bastiaanssen et al.*, 1998a, 1998b; *Su*, 2002; *Kalma and Jupp*, 1990] have employed thermal IR–based land surface temperature (LST) for regional ET monitoring. Thermal IR–based LST data are available only for clear-sky conditions and Surface Energy Balance (SEB) models that use LST to estimate ET are highly sensitive to error in LST [*Cleugh et al.*, 2007]. The RS-ET model [*Mu et al.*, 2007b] uses GMAO daily surface meteorology with MODIS land cover, albedo, LAI, and Enhanced Vegetation Index (EVI) inputs for regional ET mapping and monitoring. At high northern latitudes, Thermal IR observations are strongly constrained by cloud cover and atmospheric aerosols, while GMAO meteorological data have relatively coarse spatial resolution (1.00 × 1.25 degree) and exhibit significant error relative to surface observations. Alternatively, brightness temperature information from satellite microwave radiometers are sensitive to surface temperature and moisture conditions [*Jones et al.*, 2007] and are relatively unaffected by low solar illumination, cloud cover, smoke, and atmospheric aerosol effects. Twice-daily observations at high latitudes (>50°N) are available from polar-orbiting platforms such as the Advanced Microwave Scanning Radiometer on EOS (AMSR-E) currently operating with MODIS on the NASA EOS Aqua satellite. *Jones et al.* [2007] applied AMSR-E observations for retrieval of daily soil temperatures (<5 cm depth) across a regional network of boreal forest, grassland and tundra sites. Strong correlations between satellite microwave brightness temperatures and surface air temperature observations have also been noted for boreal Arctic regions [*Jones et al.*, 2007; *Pulliainen et al.*, 1997]. Humidity of the troposphere has been derived from thermal infrared and microwave sounding information from AIRS/ AMSU-A [*Fetzer et al.*, 2003]. Surface humidity has also been derived using land surface temperatures from AMSR-E

[*Jones et al.*, 2007] and MODIS LST [*Hashimoto et al.*, 2008]. Surface ET estimates from microwave-derived soil moisture and thermal IR information have previously been explored by *Chanzy and Kustas* [1994]. These studies indicate that surface temperature and moisture information, which is closely coupled with latent and sensible heat fluxes, may be provided by satellite microwave radiometers such as AMSR-E for remote sensing–based ET models.

[6] In this study the RS-ET method is applied to assess spatial and seasonal patterns in ET across the pan-Arctic domain above 50°N. The RS-ET algorithm is compared with tower-based ET and meteorological observations across a North American regional network of tundra and boreal forest and grassland study sites by employing three alternate sets of driving daily meteorological data: (1) local weather station observations of baseline daily meteorology, (2) surface temperature (minimum daily and daily average air temperatures) and relative humidity (vapor pressure deficit) information derived from AMSR-E, and (3) GMAO reanalysis surface meteorology. The ET estimates produced from each meteorological data set are compared with eddy covariance flux tower-based ET observations at six boreal Arctic tower sites over the 2000–2004 period to assess sensitivity of the RS-ET results to alternate meteorology inputs, and to test the performance of the global RS-ET model to estimate ET relative to tower observations. The purpose of this study is to (1) quantify spatial variability in seasonal and annual ET for the pan-Arctic domain, (2) explore the sensitivity of ET predictions to model errors introduced from alternative meteorological drivers across a transect of increasing surface control to evaporation, and (3) test the feasibility of remotely sensed microwave meteorology to complement current reanalysis inputs. The daily flux of ET can be expressed in equivalent units of both energy (W m^{-2}) and water (kg m^{-2} or mm s^{-1}). The conversion from latent energy fluxes (LE, W m^{-2}) to ET (mm s^{-1}) is ET = LE/λ, where λ is the latent heat of evaporation, which varies with temperature. For this investigation we compared mean daily LE rates between tower measurements and corresponding RS-ET model results for the six tower sites. We also evaluated spatial and temporal patterns in cumulative monthly and annual ET expressed as water equivalent depth (mm yr^{-1} and mm month^{-1}).

2. Eddy Flux Towers

[7] Model performance was assessed across a North American latitudinal transect (>50°N) of six eddy covariance flux towers representing grassland, boreal forest and tundra biomes. The six study sites represent four distinct vegetation types (Table 1 and Figure 1) including coastal lowland wet sedge tundra, boreal evergreen needleleaf forest, boreal deciduous broadleaf forest, and northern temperate grassland. Wet sedge tundra dominates in moist, poorly drained lowland and coastal areas. Coastal wet sedge tundra is represented by the Barrow (BRW) and Atqasuk (ATQ) sites and is characterized by low topography and a shallow water table with numerous thaw lakes. The vegetation is predominantly composed of low-growing sedges and mosses, interspersed with areas of shallow standing water. Soils are highly organic and consist of a shallow active layer that thaws each growing season and is underlain by continuous permafrost [*Oechel et al.*, 2000]. The BRW site
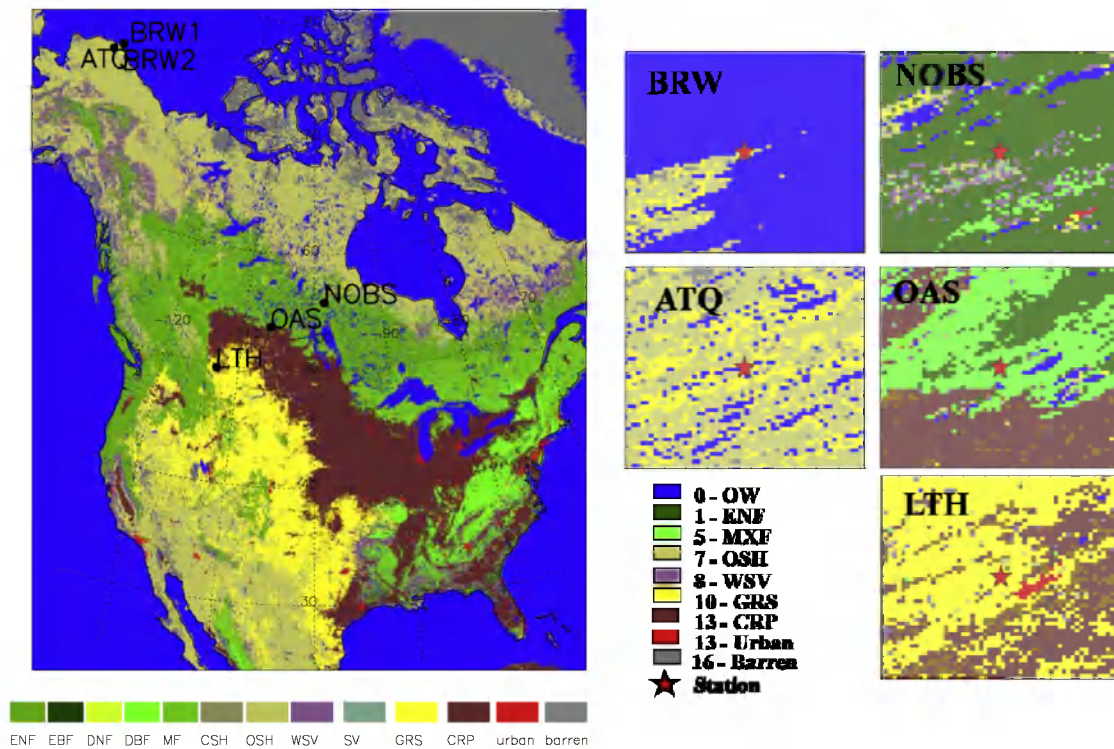
Figure 1. Distribution of the six eddy flux tower sites and the corresponding MODIS 12C1 type 2 land cover (UMD LC). ENF, evergreen needle forest; EBF, evergreen broadleaf forest; DNF, deciduous needle forest; DBF, deciduous broadleaf forest; MF, mixed forest; CSH, closed shrublands; OSH, open shrublands; WSV, woody savannas; SV, savannas; GRS, grassland; CRP, cropland; urban, urbanized; barren, barren or sparsely vegetated land. Areas in blue represent open water and other nonvegetated surfaces.

window contains two flux towers representing relatively productive (BRW$_1$) and less productive (BRW$_2$) tundra. The BRW$_1$ tower is located along the edge of a drained coastal lagoon with a greater proportion of standing water relative to the adjacent BRW$_2$ tower footprint [*Harazono et al.*, 2003; *Oechel et al.*, 1998]. Detailed classifications of land cover heterogeneity of the Barrow region indicate that drained thaw lake basins similar to the BRW$_1$ tower footprint occupy much of the Arctic Coastal Plain [*Hinkel et al.*, 2003]. Owing to the large proportion of water surface at the BRW and ATQ towers, ET is mainly composed of evaporation from both open water and wet soil vegetation surfaces. The Northern Old Black Spruce (NOBS) tower site is dominated by mature black spruce (*Picea mariana*) forest with a canopy height of 10–13 m, low topographic

relief, with understory composed of mosses (*Pleurozium* and *Sphagnum* spp.) overlying discontinuous permafrost [*Dunn*, 2006]. The Old Aspen (OAS) tower site is dominated by mature aspen (*Populus tremuloides*) forest with a mean canopy height of 21 m, an understory composed of hazelnut (*Corylus cornuta* Marsh.) and low topographic relief [*Griffis et al.*, 2004].

[8] Subgrid-scale heterogeneity in surface meteorology within the relatively coarse GMAO (1.00 × 1.25 degree) and AMSR-E (60 × 60 km) footprints may result in large differences between satellite remote sensing and tower-based ET estimates that reflect finer-scale land cover, moisture, and temperature patterns (sections 4.1 and 4.2). A MODIS 1-km resolution global land cover type 2 classification (UMD land cover classification) was used to

Table 1. Locations, Abbreviations, Latitude, Longitude, Time Period and Annual Vegetation Information at the Tower Sites[a]

Site	Abbreviation	Latitude	Longitude	Year	LAI	EVI	MA T	MA VPD	UMD LC	Tower LC
Barrow, AK (1)[b]	BRW$_1$	71.32	−156.62	2000–2003	0.91	0.30	3.2	0.10	OSH, GRS	Wet-sedge Tundra
Barrow, AK (2)[b]	BRW$_2$	71.32	−156.62	2000–2002	0.71	0.21	−	−	OSH, GRS	Wet-sedge Tundra
Atqasuk, AK	ATQ	70.47	−157.41	2000–2003	0.83	0.18	6.7	0.23	OSH, GRS	Wet-sedge Tundra
NSA-OBS, Manitoba, CN	NOBS	55.88	−98.48	2000–2004	2.28	0.26	13.1	1.17	ENF	Boreal spruce forest
SSA-OAS, Sask., CN	OAS	53.63	−106.20	2002–2004	2.48	0.28	11.6	0.69	MF	Boreal aspen forest
Lethbridge, Alberta, CN	LTH	49.71	−112.94	2002–2004	0.50	0.19	14.9	1.15	GRS	Grassland

[a]LAI, annual mean MODIS LAI; EVI, annual mean MODIS EVI; MA T, annual mean day-time air temperature in °C; MA VPD, annual mean day-time vapor pressure deficit in kPa; UMD LC, MODIS land cover type 2 within the 3 × 3 km windows overlying each tower site; Tower LC, the dominant vegetation community of within each 1 km^2 tower footprint; ENF, evergreen needle forest; MF, mixed forest; OSH, open shrublands; GRS, grassland.
[b]BRW$_1$ and BRW$_2$ are located within 2 km of each other and represent contrasting moisture conditions [*Engstrom et al.*, 2006]. Insufficient data were available to calculate MA T and MA VPD for BRW$_2$.
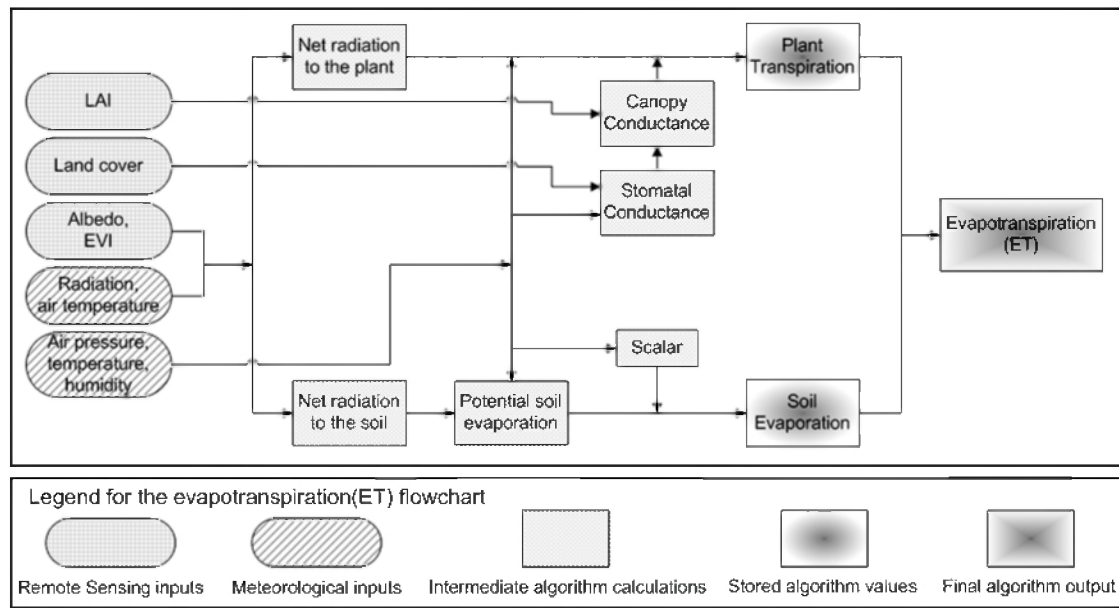
Figure 2. Flowchart showing the logic behind the MODIS ET Algorithm for calculating daily MODIS ET [*Mu et al.*, 2007b, Figure 1].

assess land cover attributes within 60×60 km windows centered on each study site location (Figure 1) [*Jones*, 2007; *Oak Ridge National Laboratory Distributed Active Archive Center*, 2006]. These regional windows are approximately of the same resolution as the AMSR-E sensor footprint at 6.9 GHz frequency (60 km $\times$ 60 km). The BRW and ATQ sites contained 87% and 12% respective open water coverage. The bulk of open water present at BRW is represented by the Arctic Ocean, while open water at ATQ is composed of numerous thaw lakes. The NOBS and OAS site windows were composed of approximately 9% and 8% open water, respectively, while Lethbridge (LTH) had <1% open water. Tundra vegetation is identified as either shrubland or grassland by the UMD land cover classification; open shrubland occupied approximately 17% of the BRW window, while grassland occupied from 60% of the ATQ window to <1% of the other tundra site windows [*Jones*, 2007]. Although the two towers at BRW (BRW$_1$ and BRW$_2$) are located about 2 km apart, they represent contrasting moisture conditions [*Engstrom et al.*, 2006]. BRW$_1$ (71.3225°N, 156.6259°W) is relatively productive with an average LAI of 0.91 and 0.71 for BRW$_2$ (71.3201°N, 156.6223°W) (Table 1). Cropland and grassland were dominant land cover types for LTH, occupying 59% and 34% of the window, respectively. Evergreen needleleaf forest was dominant at NOBS (80%), but was also present at OAS (25%). The OAS window also had significant proportions of mixed coniferous and deciduous forest (28%) and cropland (39%). The MODIS land cover map showed urban areas within the LTH and NOBS windows, but this cover type represented <1% of the total window area.

3. Methodology

3.1. Description of the RS-ET Algorithm

[9] The RS-ET algorithm of *Mu et al.* [2007b] was developed from *Cleugh et al.* [2007] using a Penman-Monteith (P-M) approach [*Monteith*, 1964] and MODIS

sensor data. A flowchart of the RS-ET algorithm structure and associated model inputs and outputs is presented in Figure 2 [*Mu et al.*, 2007b]. The ET term is the sum of plant transpiration and soil evaporation. The daily net incoming radiation is linearly partitioned between the canopy and soil surface using the vegetation cover fraction (F_C) derived from the MODIS EVI (see Appendix A).

[10] Canopy transpiration is constrained by the surface resistance (s m^{-1}) term, which is the inverse of canopy conductance to water vapor exchange with the atmosphere. Surface resistance is calculated on the basis of daily minimum air temperature (Tmin) and vapor pressure deficit (VPD). We calculate the environmental constraints to ET by minimum air temperature (Tmin) and VPD as

$$m(T\min) =$$
$$\begin{cases} 1.0 & T\min \geq T\min\_open \\ \dfrac{T\min - T\min\_close}{T\min\_open - T\min\_close} & T\min\_close < T\min < T\min\_open \\ 0.1 & T\min \leq T\min\_close \end{cases}$$
$$(1)$$

$$m(VPD) =$$
$$\begin{cases} 1.0 & VPD \leq VPD\_open \\ \dfrac{VPD\_close - VPD}{VPD\_close - VPD\_open} & VPD\_open < VPD < VPD\_close \\ 0.1 & VPD \geq VPD\_close \end{cases}$$

where *close* indicates nearly complete inhibition (full stomatal closure) and *open* indicates no inhibition to canopy transpiration [*Mu et al.*, 2007b, Table 1]. When Tmin is lower than the threshold value Tmin_close, or VPD is higher than the threshold VPD_close, temperature or water stress will cause stomata to close almost completely, halting canopy transpiration. On the other hand, when Tmin is warmer than Tmin_open, and VPD is lower than VPD_open, there will be no temperature or water stress limitations on

transpiration. The multipliers range linearly from 0.1 (nearly total inhibition of stomatal conductance and transpiration) to 1 (no inhibition) and vary by land cover type as defined in a general Biome Properties Look-Up Table (BPLUT) [*Mu et al.*, 2007b, Table 1]. A similar BPLUT is used to define general biophysical properties for land cover classes in the NASA MODIS (MOD17) production efficiency model–based global mapping of GPP and NPP [*Running et al.*, 2004; *Zhao et al.*, 2005; F. A. Heinsch et al., User's Guide: GPP and NPP (MOD17A2/A3) Products, NASA MODIS Land Algorithm, available at http://ntsg.umt.edu/modis/ MOD17UsersGuide.pdf].

[11] Soil evaporation is calculated as a nonlinear reduction from estimated soil evaporation under potential (no moisture limitation) conditions using the Penman-Monteith equation (A1). The actual soil evaporation (A7) is calculated as a reduction from potential conditions following *Fisher et al.* [2008] with parameters fitted to the tower LE observations from the global RS-ET algorithm application of *Mu et al.* [2007b]. This approach is based on the complementary relationship hypothesis [*Bouchet*, 1963], where VPD and relative humidity are used as a surrogate for soil wetness. This allows an implicit treatment of the effect of soil water availability in the RS-ET algorithm as accurate soil moisture information is not currently available for continental regions. The lower atmosphere is highly responsive to land surface conditions [*Bouchet*, 1963; *Morton*, 1983], and VPD has been used as an indicator of environmental water stress at the regional scales represented by global satellite remote sensing [*Running and Nemani*, 1988; *Granger and Gray*, 1989]. *Mu et al.* [2007a] found that VPD alone captured interannual variability in vegetation water stress from both the atmosphere and soil over much of China and the conterminous U.S., though it may fail to capture seasonal water stress in dry regions experiencing strong summer monsoons.

[12] *Mu et al.* [2007b] evaluated the RS-ET algorithm at 19 AmeriFlux eddy covariance flux tower sites distributed across North America. Daily RS-ET derived fluxes for 2001 were obtained using tower observed meteorology and alternative GMAO surface meteorological inputs. The root mean square error (RMSE) of differences between tower flux measurements of 8-day mean LE- and RS-ET-based results averaged over the 19 towers was 27.3 W m^{-2} and 29.5 W m^{-2} (for ET, RMSE is 0.61 mm d^{-1} and 0.68 mm d^{-1}, respectively) using tower and GMAO meteorological inputs, respectively. The average bias of the RS-ET LE results relative to the tower measurements was -5.8 W m^{-2} using tower meteorological inputs and -1.3 W m^{-2} using GMAO inputs.

[13] For this investigation, the RS-ET model was applied at the six boreal Arctic tower sites (Table 1) and multiyear (2000–04) time period where data were available by extracting 3 × 3 km^2 cutouts of MODIS 1-km resolution LAI, land cover and EVI, and MODIS 0.05° resolution albedo time series surrounding each site location as model inputs. The AMSR-E derived meteorological data are representative of conditions within an approximate 60 km × 60 km (6.9 GHz) resolution footprint (the actual footprints are egg shaped at 43 km × 73 km) surrounding each tower location (see section 3.4). Daily LE was estimated on a grid cell by cell basis within each site window using the MODIS

data series and three alternate sets of daily surface meteorology inputs. The daily LE results were then spatially averaged within each site window and compared with corresponding daily tower observations. The RS-ET model was also applied with daily MODIS and GMAO surface meteorological inputs to estimate monthly and annual ET for all land areas above 50°N to assess regional patterns and temporal variability in ET across the pan-Arctic domain.

3.2. Input MODIS Data

[14] Continuous daily time series of MODIS 1-km resolution LAI, NDVI, EVI, and 0.05° resolution albedo inputs to the RS-ET model were constructed for each 3 × 3 km^2 site window. These daily time series were constructed by filling in erroneous quality control (QC) flagged or missing data values through temporal linear interpolation of adjacent good quality data following *Zhao et al.* [2005]. The 8-day MODIS LAI (MOD15A2) [*Myneni et al.*, 2002] and 16-day MODIS NDVI and EVI (MOD13A2) [*Huete et al.*, 2002, 2006] time series contain some cloud-contaminated or missing data. According to the MOD15A2 quality assessment scheme provided by *Myneni et al.* [2002], LAI values retrieved by the main algorithm (i.e., Radiation Transfer process, denoted as RT) are most reliable, and those retrieved by the backup algorithm (i.e., the empirical relationship between FPAR/LAI and NDVI) are less reliable because the backup algorithm is employed mostly when cloud cover, strong atmospheric effects, or snow/ice are detected. For this investigation, only good quality RT retrievals were used to construct complete LAI time series. We used the 10th band of the White-Sky Albedo from the 0.05° resolution 16-day MODIS MOD43C1 BRDF product [*Lucht et al.*, 2000; *Schaaf et al.*, 2002] (http://www-modis. bu.edu/brdf/userguide/cmgalbedo.html) to define surface albedo. These data were used with GMAO solar radiation to determine mean daily net solar radiation inputs for the RS-ET model calculations. The MODIS 8-day 1-km UMD land cover product was also used to define general land cover properties of the 9 pixels surrounding each site location.

3.3. Operational GMAO Meteorology

[15] The 1.00° × 1.25° resolution of GMAO reanalysis meteorological data is much coarser than each 1-km MODIS pixel. *Zhao et al.* [2005] found that, in the Collection 4 MOD17 algorithm (MOD17), adjacent 1-km pixels within each 1.00° × 1.25° GMAO grid cell inherited the same meteorological data, creating a noticeable GMAO footprint [*Zhao et al.*, 2005, Figures 1a and 1c]. To mitigate these effects, we employed a spatial nonlinear interpolation of coarse resolution GMAO data to each 1-km^2 MODIS pixel using the four GMAO cells surrounding a given pixel as proposed by *Zhao et al.* [2005]. Daily ET was then computed across the pan-Arctic domain over 2000–2006 and for each tower site over 2000–2004 using the corresponding interpolated GMAO daily time series.

3.4. AMSR-E Meteorology

[16] Daily brightness temperature (Tb) measurements from AMSR-E were used to obtain alternate surface meteorological inputs to the RS-ET model for temperature (daily minimum and daytime average air temperatures) and humidity (VPD). The AMSR-E sensor operates with MODIS on the

NASA EOS Aqua satellite platform, which was launched in May of 2002. The AMSR-E sensor measures multifrequency brightness temperatures at 6.9, 10.7, 18.7, 23.8, 36.5, and 89 GHz wavelengths, for vertical and horizontal polarizations. Aqua is polar orbiting with 1 A.M./P.M. equatorial crossing times, providing multiple acquisitions twice daily in polar regions (>50°N). Observations therefore occur between 2 and 4 A.M. (P.M.) local time for the descending (ascending) overpass. We extracted daily time series observations from the L2A swath data product [*Ashcroft and Wentz*, 1999; *Jones et al.*, 2007] centered over each study site location. The sensor footprint varies with measurement frequency from approximately 5-km (89 GHz) to 60-km (6.9 GHz) spatial resolution. The L2A product includes all frequencies resampled to the 6.9 GHz native resolution and therefore can be considered representative of a ~60 km × 60 km spatial resolution.

[17] Previous studies have used microwave radiometry to derive air and soil temperatures in arctic and boreal regions. *Pulliainen et al.* [1997] compared regression and radiative transfer methods for determining air temperature from the Special Sensor Microwave/Imager (SSM/I) in Finland. *Fily et al.* [2003] applied a polarization difference method to retrieve screen height air temperatures in northern Canada. *Jones et al.* [2007] developed methods to retrieve surface (<10 cm depth) soil temperatures from AMSR-E daily Tb time series for boreal forest and Arctic tundra biophysical monitoring sites across Alaska and Canada. The seasonal pattern of microwave emission and relative accuracy of the soil temperature retrievals had an overall RMSE of 3.1–3.9 K, with larger error occurring in winter, during periods with dynamic snow cover and freeze–thaw state conditions.

[18] For this investigation we employed an empirical multiple regression approach for retrieval of daily minimum (*T*min) and average day-time (*T*day) screen-height (≈2 m) air temperatures from AMSR-E multifrequency Tb time series for each site location. The equation uses vertically polarized Tb data at 10.7, 18.7, and 89 GHz frequencies, and H/V polarization ratios of the 6.9 GHz and 89 GHz channels. Empirical relationships were established between surface weather station–based air temperature time series at each site and corresponding AMSR-E Tb measurements; descending (1 AM) overpass Tb data were fit to *T*min and ascending (1 PM) overpass Tb data were fit to maximum daily air temperature (*T*max) measurements for each site. Thawed season data from 2002 to 2003 (BRW$_2$ was excluded from this phase owing to limited data coverage) were used for fitting model parameters, whereas 2004 was reserved for the accuracy assessment. The thawed season was defined by temporal shifts in AMSR-E brightness temperatures corresponding to the transition from snow covered frozen conditions to predominantly thawed conditions [*Jones et al.*, 2007]. The *T*day term was estimated from daily *T*min and *T*max by assuming a simple sinusoidal temperature curve. Daily average VPD was estimated from *T*min and *T*day on the basis of the assumption that *T*min is equivalent to the daily dew point [*Kimball et al.*, 1997]. This assumption generally holds for boreal and arctic regions under nonfrozen conditions, where relatively abundant surface water provides a reservoir for evaporation and low nighttime temperatures constrain absolute humidity through dewfall.

3.5. Tower Meteorology and Flux Data

[19] The boreal Arctic study sites contain operational eddy covariance flux tower instrumentation for measuring land-atmosphere exchanges of energy, carbon dioxide and moisture as well as temperature and the 3D components of wind speed above the canopy [*Rana and Katerji*, 2000; *Baldocchi et al.*, 2001]. The automated tower flux measurements are collected 20 times per second and are averaged every 30 min. Water vapor concentration is measured along the height of the tower using either closed or open path infrared gas analyzers and flux is inferred from wind speeds measured by three-dimensional sonic anemometers. Energy balance closure is typically underestimated by 10–30% for such systems indicating some systematic uncertainty in energy flux estimates [*Baldocchi*, 2008]. The flux tower meteorological data were used to assess accuracy in GMAO/AMSR-E meteorology and model LE (ET) relative to local site observations. The temporal period of tower measurements for this investigation included the years 2000–2004 where available (Table 1). The BRW$_2$ data was only available for 2000–2002. The year 2003 represented the most continuous coverage of incoming solar radiation; therefore this year's data was used for comparison to the GMAO solar radiation. The reported half-hourly data was aggregated to a daily time step for this investigation. We only selected days with complete half-hourly tower LE measurement series to compare with RS-ET model results. The tower observations employed in this study were LE and the incoming solar radiation (Rs; W m^{-2}), minimum daily air temperature (*T*min; °C), daytime average air temperature (*T*day; °C), and daytime average vapor pressure deficit (VPD; kPa). Daytime averages were defined as the average over the period of the day when Rs > 0. The net incoming solar radiation (Rsn) is calculated using Rs and surface albedo.

4. Results

4.1. Assessment of GMAO and AMSR-E Meteorology Relative to Tower Observations

[20] Relations between GMAO and AMSR-E meteorological estimates relative to corresponding daily tower observations from the 6 tower sites are displayed in Figure 3. The RMSE accuracy of air temperature and VPD estimates relative to tower observations were on the order of 2.8–3.4°C and 0.3–0.4 kPa. The AMSR-E-based *T*min and *T*day retrievals showed generally smaller (~0.4°C) errors relative to GMAO derived temperatures. The AMSR-E results tended to over predict *T*day by 1.5°C, while the GMAO reanalysis tended to over predict *T*min by 1.7°C. The AMSR-E results also produced more favorable estimates of VPD with RMSE of 0.30 kPa compared to 0.40 kPa from the GMAO data. The AMSR-E VPD results showed a dry bias relative to tower observations by ~0.2–0.3 kPa for wet atmospheric conditions (VPD < 0.5 kPa) and a wet bias during dry (VPD ≥ 0.5 kPa) conditions. The RMSE and mean residual errors were generally consistent with or smaller than GMAO derived results (Figure 3). The GMAO-based Rsn inputs had an RMSE accuracy of 64.9 W m^{-2} relative to tower observations. GMAO tended to under predict Rsn relative to local tower conditions with mean residual error in Rsn from 3.6 to 43.3 W m^{-2}, even though
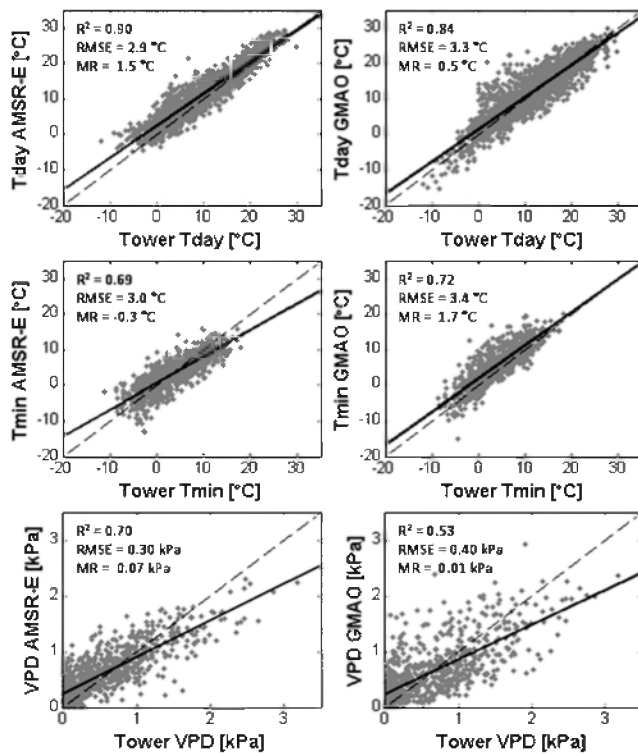
Figure 3. Comparison of AMSR-E and GMAO meteorological variables to tower observations at all sites; solid lines represent the linear least squares regression line, while dashed lines represent a 1:1 relationship. See Table 2 for site-specific results, temporal coverage of data, and statistic abbreviations.

the GMAO product accounted for approximately 70 percent of the variance in tower Rsn observations.

[21] Site specific relationships between GMAO and AMSR-E meteorology inputs and tower observations are summarized in Table 2. The RMSE between tower- and AMSR-E-based temperatures for individual sites ranged from 1.9°C to 3.3°C for Tmin and 2.1°C to 3.4°C for Tday. The GMAO temperature RMSE results ranged from 2.1°C to 4.9°C for Tmin and 2.1°C to 5.6°C for Tday. Both methods showed the greatest temperature error at the BRW_1 site, likely due to the coastal location of the BRW_1 towers and large amount of open water in both the GMAO and AMSR-E footprints. The BRW_1 and BRW_2 locations are located within 2 km of each other and tower observations at the two locations agree to within 0.4–0.5°C for air temperatures and 0.02 kPa for VPD. The largest discrepancy between the two data sets was for Rsn at BRW_2, which was approximately 34 W m^{-2} higher than the BRW_1 observations. The GMAO and AMSR-E results also showed a dry bias and over predicted VPD at BRW_1, BRW_2, and ATQ, all sites located within 50 km of the coast in low relief where tower observations are likely influenced by marine advection and evaporation from locally abundant freshwater lakes. The GMAO and AMSR-E results showed a wet bias in daily VPD relative to tower observations at the NOBS and LTH sites. These biases were 0.34 and 0.03 kPa for GMAO (0.37 and 0.18 kPa for AMSR-E), respectively. The RMSE differences between GMAO-based Rsn and individual site observations varied from 43.9 to 74.5 W m^{-2} and generally underestimated radiation at higher-latitude locations (>55°N, all sites from NOBS northward), but over estimated radiation at lower-latitude sites (OAS and LTH).

[22] Differences between GMAO and AMSR-E meteorological inputs relative to tower observations were largely attributed to algorithm representation, which includes sub-grid-scale spatial heterogeneity in surface meteorology within the relatively coarse footprints of the satellite sensor and reanalysis products and process parameterization. The tower observations represent local conditions within a relatively small area (approx. ≤1 km^2) surrounding each tower. In contrast, the AMSR-E results represent an approximate 60 km × 60 km footprint, while GMAO data are spatially interpolated from coarse (1° × 1.25°) resolution (section 3.2). Despite these scale differences, both GMAO and AMSR-E derived daily meteorology inputs compared favorably with surface observations over a wide range of environmental conditions represented by the boreal Arctic regional tower transect. The AMSR-E-based temperature and VPD results also generally compared more favorably to the tower observations than the GMAO results, due, in part, to finer spatial resolution of the AMSR-E footprint relative to the GMAO reanalysis. The wet bias in AMSR-E derived VPD estimates at NOBS and LTH is attributed to Tmin departure from dew point temperature (Tdew) at these two locations.

4.2. Validation of RS-ET Algorithm at Tower Sites

[23] The average RS-ET-based LE and meteorological data of the 3 × 3 1-km pixels surrounding each study site were compared with tower LE observations. First, we compared seasonal results between the tower LE observations and LE estimates driven by the three sets of meteorology and MODIS input data. The seasonal patterns of tower observed and model estimated daily LE are presented in Figure 4 for all the six sites over the time period with available data. The LE results derived from the three alternate sets of meteorological inputs generally capture seasonality of the tower observed LE. Corresponding scatterplots and 1:1 relations between RS-ET derived LE and tower observations (Figure 4) indicate that the LE estimates show similar magnitudes relative to the tower-based LE observations except for LTH. Both model and observed LE time series ranged between characteristically high LE rates during vegetation growing seasons and seasonally low rates in winter. The model results generally showed less year-to-year LE variability than tower-based fluxes. For example, tower LE observations at the NOBS site were relatively low in the summer of 2001 compared to other years, while model LE estimates from site and GMAO meteorology inputs were much higher than tower LE observations, and were nearly as high as 2002 and 2003 summer fluxes. The magnitudes of model LE estimates in the other years were closer to the tower observations, and were lower in the summers of 2000 and 2004 than in the summers of 2002 and 2003.

[24] Figure 4 shows strong seasonal variation in LE at the six tower sites. Part of the LE seasonality is driven by variation in net radiation during the year due to solar forcing. We examined the relative skill of the RS-ET model with respect to the *Priestley and Taylor* [1972] model–based equilibrium evaporation since the latter only depends

Table 2. Site Specific Statistics for the Comparison of AMSR-E and GMAO Meteorological Variables to Tower Observations[a]

	R^2	RMSE	MAE	MR	N
			BRW₁		
*T*min	0.50(0.43)	4.5(3.3)	3.4(2.6)	2.5(−0.4)	111(111)
*T*day	0.55(0.58)	5.6(3.4)	4.3(2.9)	3.6(2.0.)	111(111)
VPD	0.08(0.00)	0.37(0.25)	0.25(0.19)	0.23(0.17)	113(113)
Rsn	0.56–	43.9–	35.3–	22.1–	70–
			BRW₂		
*T*min	0.41(0.31)	3.5(3.0)	2.6(2.6)	1.5(0.4)	103(84)
*T*day	0.51(0.56)	4.8(3.0)	3.3(2.4)	2.9(1.9)	103(81)
VPD	0.24(0.1)	0.34(0.16)	0.2(0.14)	0.18(0.12)	103(81)
Rsn	0.60–	45.5–	35.8–	15.6–	103–
			ATQ		
*T*min	0.84(0.84)	2.7(1.9)	2.0(1.5)	1.6(−0.9)	101(100)
*T*day	0.84(0.88)	3.4(2.1)	2.7(1.7)	2.0(1.3)	101(100)
VPD	0.46(0.57)	0.43(0.26)	0.31(0.22)	0.29(0.2)	100(99)
Rsn	0.40–	54.45–	40.4–	13.5–	78–
			NOBS		
*T*min	0.64(0.78)	4.9(3.0)	4.1(2.4)	3.7(2.1)	141(129)
*T*day	0.86(0.94)	2.2(2.4)	1.8(2.1)	0.5(2.0)	140(118)
VPD	0.75(0.74)	0.46(0.45)	0.4(0.4)	−0.4(−0.3)	117(99)
Rsn	0.61–	73.2–	56.35–	36.3–	161–
			OAS		
*T*min	0.89(0.84)	2.1(2.6)	1.6(2.1)	0.2(−0.7)	198(187)
*T*day	0.92(0.94)	2.1(2.5)	1.6(1.8)	0.7(1.5)	198(167)
VPD	0.66(0.74)	0.29(0.22)	0.2(0.18)	0.1(0.06)	198(167)
Rsn	0.62–	74.5–	56.2–	33.6–	172–
			LTH		
*T*min	0.8(0.79)	2.9(2.8)	2.3(2.2)	1.5(0.5)	220(187)
*T*day	0.79(0.78)	3.5(3.4)	2.8(2.5)	−1.8(1.5)	220(159)
VPD	0.47(0.69)	0.49(0.34)	0.39(0.26)	−0.18(−0.03)	216(157)
Rsn	0.67–	68.3–	53.8–	43.3–	212–

[a]GMAO, Global Modeling and Assimilation Office. Advanced Microwave Scanning Radiometer on EOS (AMSR-E) statistics are shown in parentheses. Temporal coverage includes thawed season for 2004 for *T*min, *T*day, and vapor pressure deficit; summer 2003 for Rsn; and 19 June to 30 September 2002 for the BRW₂ site (see sections 3.4 and 3.5). *T*min, minimum daily air temperature (°C); *T*day, daytime average air temperature (°C); VPD, vapor pressure deficit (kPa); Rsn, net incoming solar radiation (W m^{-2}); R^2, coefficient of determination; RMSE, root mean square error; MAE, mean absolute error; MR, mean residual (Estimate − Observation); N, sample size in days.

on radiation and temperature, with minimal vegetation control on ET:

$$\lambda E = \frac{1.26 s A}{s + \gamma} \qquad (2)$$

where λE (W m^{-2}) is the latent heat flux and λ (J kg^{-1}) is the latent heat of evaporation; s (Pa K^{-1}) and is the slope of the curve relating saturated water vapor pressure to temperature; A (W m^{-2}) is available energy. γ (Pa K^{-1}) is the psychrometric constant. Figure 5 shows the RS-ET LE estimates driven by tower observed meteorology and the potential LE (PLE) calculated with equation (2) driven by the same tower observed meteorology. The RS-ET LE estimates are reduced from PLE with increases in the surface resistance to evapotranspiration. The 8-day RMSE driven by the tower meteorology data reduced from 27.6 W m^{-2} to 14.3 W m^{-2} averaged over all the six towers.

[25] The RS-ET model was developed to estimate ET operationally on a global basis using MODIS vegetation and GMAO surface meteorological inputs. The MODIS LAI and EVI and BRDF products are produced at respective 8-day and 16-day intervals and represent average conditions within each time period, even though these parameters likely vary within each 8- or 16-day time period. The RS-ET results were produced at 8-day intervals consistent with other NASA MODIS products and to reduce potential bias introduced by interpolating MODIS data

series to finer temporal scales. To evaluate RS-ET model performance, we calculated RMSE values, correlations (R) and mean residual biases between mean 8-day tower observations and model estimated LE derived from the three alternate meteorological data sources, including daily tower, GMAO and AMSR-E meteorological inputs. To facilitate comparisons among the 8-day LE results, we only compared results having complete sets of daily observations across all three data sets including tower LE observations, and tower, GMAO and AMSR-E derived meteorology. For NOBS and OAS over the 2002–2004 AMSR-E data collection period, model results derived from tower observed meteorology inputs can capture the seasonality and magnitude of observed LE. The correlation coefficients are 0.60 and 0.81, RMSE values for 8-day LE are 32.4 W m^{-2} and 27.2 W m^{-2}, mean residual biases are 18.1 W m^{-2} relative to average LE of 64.4 W m^{-2} and 7.9 W m^{-2} to average LE of 79.5 W m^{-2} for NOBS and OAS, respectively (Table 3 and Figure 6). Averaged over the six tower sites and all 92 8-day time periods, average LE from the tower observations is 62.1 W m^{-2}. Model-based LE results derived from site meteorology inputs for all sites and 8-day time periods produced a mean RMSE of 14.3 W m^{-2}, a correlation of 0.62, and bias of −5.3 W m^{-2} compared to tower observations. LE estimates driven by AMSR-E and GMAO meteorology inputs were very similar to the LE estimates driven by tower observed meteorology data (Table 3 and Figure 6). The 8-day RMSE and bias between the LE
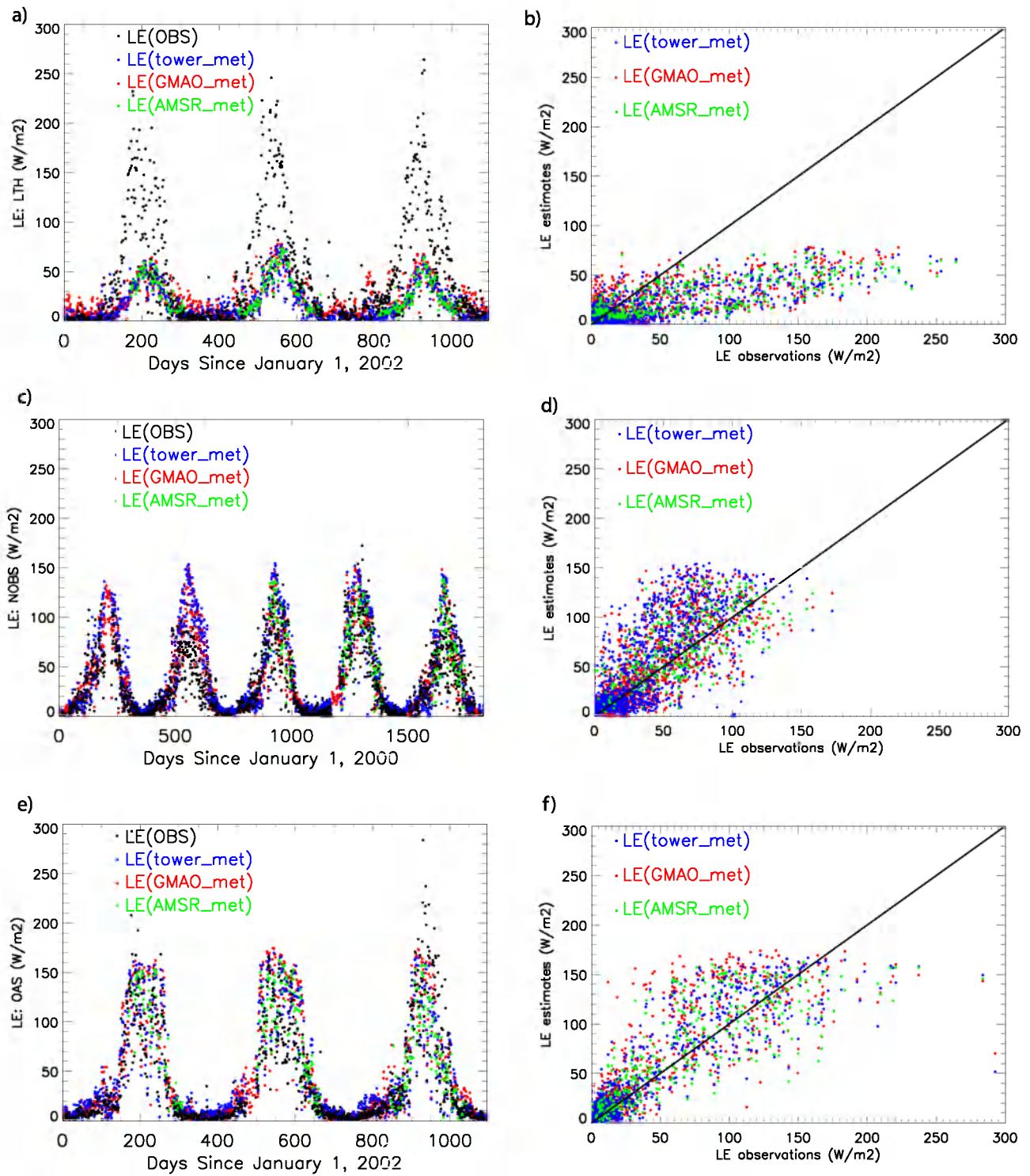
Figure 4. Comparison of daily tower ET observations (black dots, OBS) with ET estimates driven by (1) flux tower (blue dots), (2) GMAO (red dots), and (3) AMSR-E (green lines) derived from meteorological data at the LTH, NOBS, and OAS sites (Table 1 and Figure 1).

estimates and LE observations was approximately 22.6 and 9.3 percent of average 8-day LE observations, respectively.

[26] Figure 6b shows the Relative Error (RE: RMSE/ mean observed latent heat flux) (%) differences between tower observed and model estimated mean 8-day latent energy flux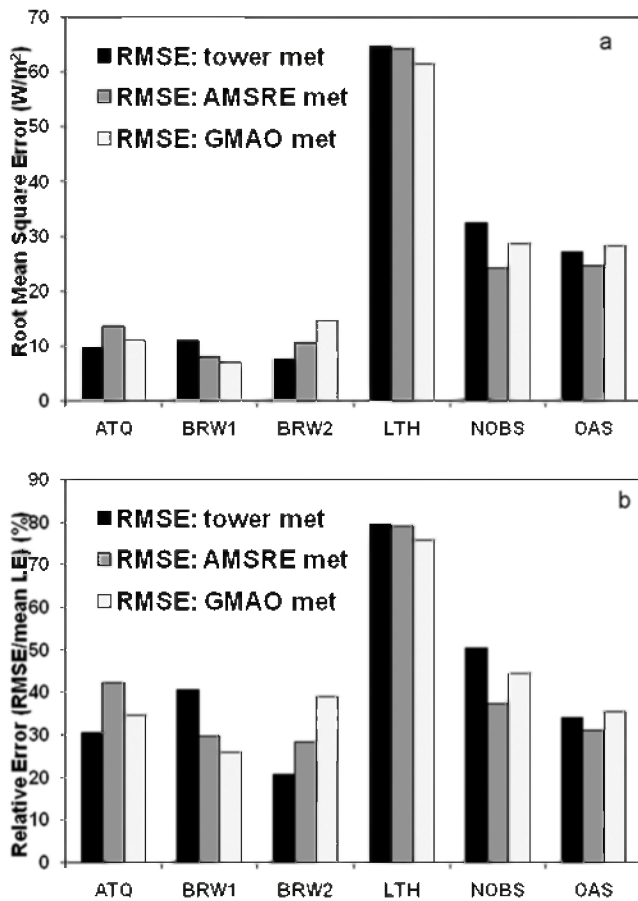es derived from the three alternate sets of meteorological data inputs (Figure 6b and Table 3). Though there are big differences in RMSE among different tower sites, the RE differences between different vegetation types are small except for LTH, because high RMSE corresponds to high LE for the forests, low RMSE and low LE for the grasslands ATQ, BRW_1 and BRW_2.
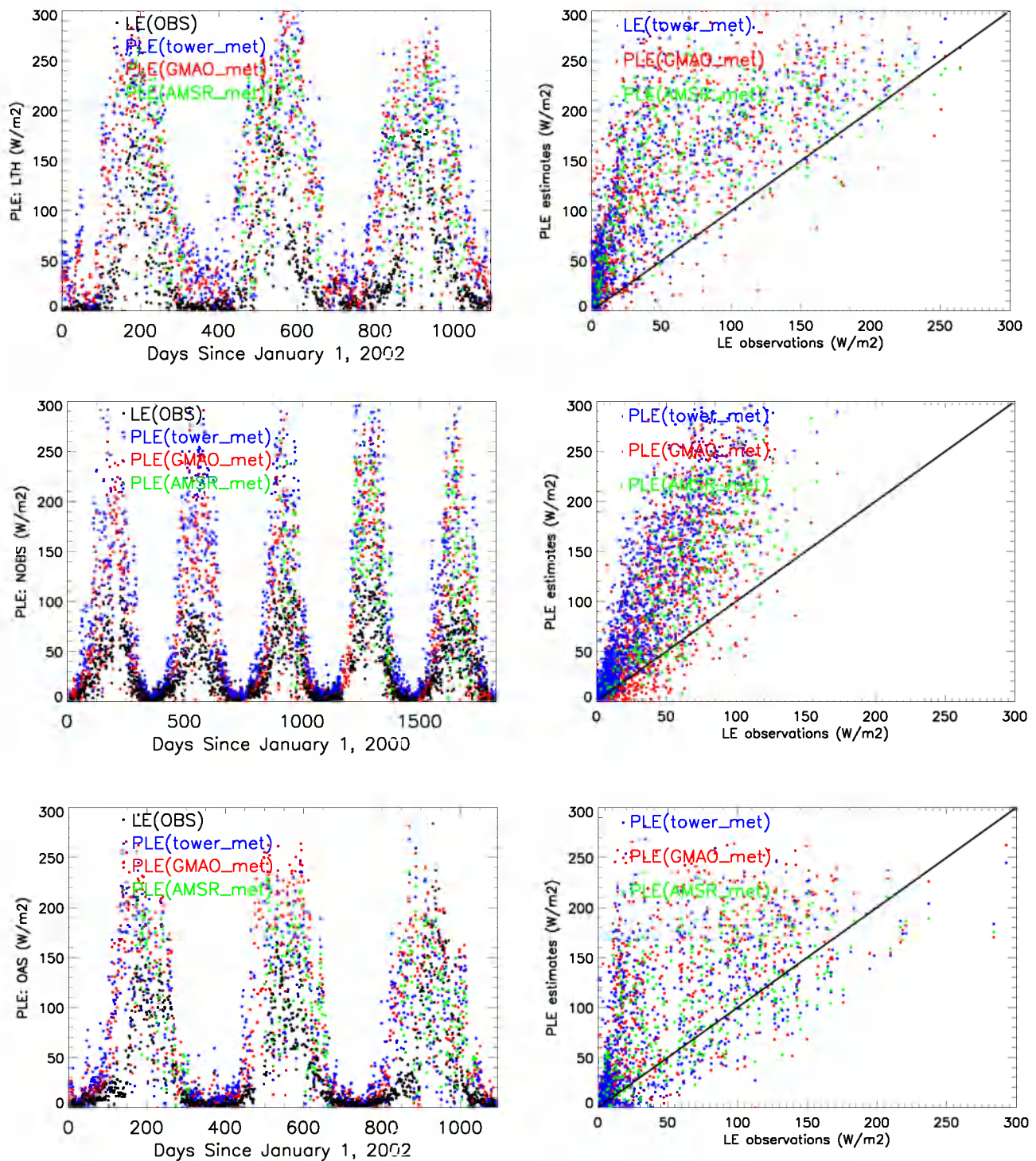
Figure 5. RS-ET LE estimates driven by tower-observed meteorology and the potential LE (PLE) calculated with Priestley-Taylor equation driven by the same tower-observed meteorology.

[27] There are several possible reasons for the high relative error at LTH. First, there may be errors associated with tower LE observations or MODIS LAI estimates at LTH. Previous tower studies indicate underestimation of the surface energy balance by 10−30% [*Baldocchi*, 2008], though the RS-ET results show a consistent underestimation of tower LE. We compared input MODIS LAI, EVI, and GMAO *T*min, daytime average temperature (*T*day), VPD, net incoming radiation (netRad) at LTH and NOBS in

Figure 7. The magnitudes of the meteorological variables at LTH and NOBS are very close. In summer, the maximum EVI at both sites is approximately 0.34, when the vegetation cover fraction is 68% using equation (A3). The net radiation allocated to plants and soil at both sites is similar according to equation (A4). Some studies have suggested that the atmospheric humidity conditions reflect the dryness of the ground surface and VPD can be used as an indicator of environmental water stress [*Morton*, 1983; *Running and*

Figure 6. (a) Root-mean-square error (RMSE, W m^{-2}) and (b) relative error (RMSE/mean LE, %) between tower observed and model estimated mean 8-day latent energy fluxes derived from the three alternate sets of meteorological data inputs.

Nemani, 1988; *Granger and Gray*, 1989; *Mu et al.*, 2007a], while water limitations on surface conductance in the RS-ET model are expressed by VPD only. In summer, when EVI at both sites approaches the seasonal maximum, the surface meteorology produces similar predicted soil evaporation (equations (A5–A7)). So the main difference between the two sites comes from plant transpiration, which is sensitive to canopy conductance, constrained by both meteorology and LAI (equations (1) and (A2)). The limitations on canopy conductance come from meteorology and LAI (equations (1) and (A2)). Owing to the similar meteorology, canopy differences between the two sites comes from LAI. Higher LAI at NOBS (Figure 7a) should result in higher canopy conductance transpiration than that at LTH, which results in higher ET (soil evaporation + plant transpiration) at NOBS. But in Figure 4, ET observations at NOBS in summer are much lower than those at LTH, which implies that ET observations or MODIS LAI estimates may contribute to the large RMSE differences at LTH. Also, as in equation (A2), C_L is set to be constant for all different vegetation types, which might cause the biases in LE estimates. Other potential contributions to tower model differences include spatial scale differences between tower footprint and landscape resolutions commensurate with GMAO and AMSR-E surface meteorological inputs and RS-ET algorithm limitations as discussed in section 4.5.

[28] There were strong correlations between LE observations at the six tower sites and model LE estimates produced from the three meteorological data sets averaged over each 8-day time period and 3 × 3 km site window. Correlation coefficients between tower LE observations and RS-ET model results were 0.62 using tower meteorology inputs; 0.67 using GMAO inputs and 0.66 using AMSR-E derived meteorological inputs. Averaged over all six tower sites and 8-day time periods with complete meteorology and LE measurement series, the RMSE differences between average LE observations and RS-ET estimates from tower, AMSR-E and GMAO meteorology inputs were 13.1, 17.2 and 12.4 percent of mean LE observations, respectively. Model results from GMAO-based meteorology inputs produced LE bias of −4.2 W m^{-2}, followed by model bias of −5.3 W m^{-2} and −7.8 W m^{-2} from respective site and AMSR-E meteorology inputs (Table 3 and Figure 6). These results and those from Table 3 indicate that RS-ET model bias was lowest using GMAO meteorology inputs, followed by tower observed and AMSR-E-based meteorology inputs. However, the RS-ET fluxes derived from the AMSR-E meteorology inputs produced the lowest RMSE relative to the other meteorological sources.

4.3. RS-ET Meteorology Error Sensitivity Analysis

[29] An error sensitivity analysis was conducted to assess the amount of error imparted to the LE estimates by RS-ET given two error levels, low and high, spanning the range in

Table 3. Comparisons of the RS-ET Estimated 8-Day Latent Heat Flux Derived Using Daily Surface Meteorological Inputs From Tower, AMSR-E, and GMAO With Observations[a]

Site	Mean	RMSE1	RE1	R1	MR1	S1	I1	RMSE2	RE2	R2	MR2	S2	I2	RMSE3	RE3	R3	MR3	S3	I3
BRW$_1$	27.31	11.1	40.7	0.53	−7.9	0.6	5.4	8.2	29.8	0.45	−5.4	0.4	10.4	7.1	25.8	0.51	−4.2	0.2	16.9
BRW$_2$	37.40	7.7	20.7	0.94	−5.3	0.7	6.2	10.6	28.5	0.88	−8.0	0.5	9.9	14.6	39.0	0.90	−12.7	0.3	9.1
ATQ	32.11	9.8	30.5	0.68	−3.9	0.4	12.6	13.6	42.3	0.44	−8.0	0.3	14.6	11.1	34.5	0.51	−2.0	0.05	23.6
NOBS	64.40	32.4	50.3	0.60	18.1	1.0	9.5	24.1	37.4	0.74	9.5	0.7	28.5	28.6	44.4	0.75	12.5	1.0	7.1
OAS	79.53	27.2	34.2	0.81	7.8	0.9	9.2	24.7	31.1	0.84	6.6	0.7	24.5	28.1	35.3	0.85	13.4	0.9	11.9
LTH	81.23	64.8	79.7	0.86	−51.1	0.2	6.4	64.3	79.1	0.83	−50.1	0.2	12.2	61.5	75.7	0.85	−46.9	0.2	11.5
Average	62.10	14.3		0.62	−5.3			13.0		0.66	−7.8			14.8		0.67	−4.2		

[a]Root Mean Square Error (RMSE), relative error (RE = RMSE/mean LE, %), mean residual (MR = Estimate − Observation), and correlation coefficient (R) between tower observations and RS-ET results for the six tower sites. Slopes (S) and intercepts (I) of the daily latent heat flux (W m^{-2}) versus daily latent heat flux (W m^{-2}) observations for the six tower sites. The RS-ET results are derived using daily surface meteorological inputs from three alternate sources: (1) tower, (2) AMSR-E, and (3) GMAO.
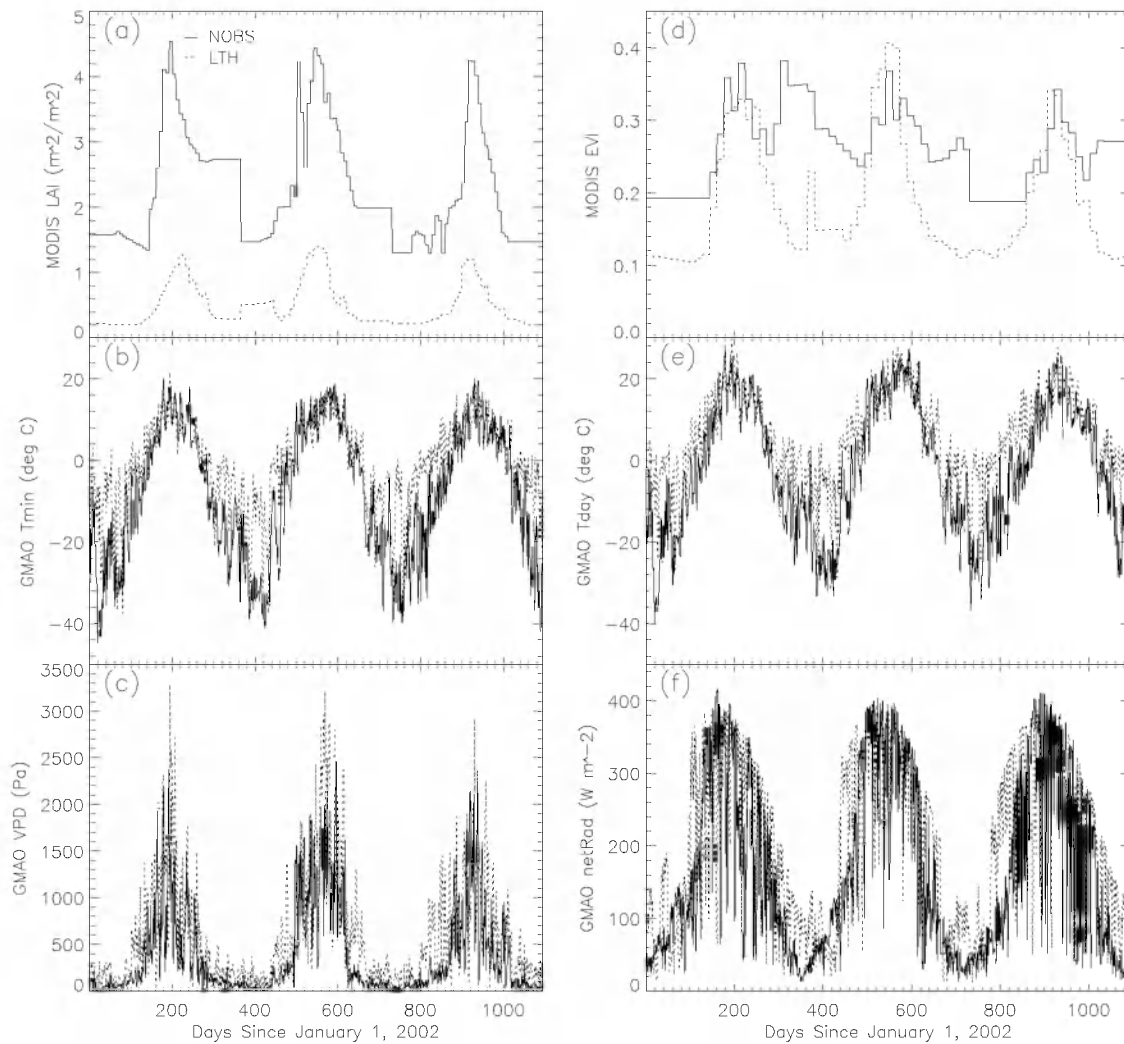
Figure 7. Comparison of input MODIS leaf area index, enhanced vegetation index, and GMAO minimum temperature (Tmin), daytime average temperature (Tday), vapor pressure deficit, and net incoming radiation at LTH and NOBS.

input temperatures (Tmin and Tmax) and net incoming solar radiation (Rsn). The two error levels give RS-ET accuracies for LE in accordance with the meteorological drivers reported from pixel to point site comparisons in section 4.1 and reported by *Jones et al.* [2007]and *Zhao et al.* [2006]. The low error scenario considered equal error of 2°C in both Tmin/Tmax and error of 50 W m^{-2} in Rsn. The high error scenario considered equal error of 4°C in both Tmin/Tmax and error of 90 W m^{-2} in Rsn. Model input parameters for the sensitivity analysis included leaf area index, Rsn, and Tdew, ranging from 1 to 5 m^2 m^{-2}, 100 to 400 W m^{-2}, and 0 to 20°C, respectively. The Tmax values ranged between Tdew and 35°C and produced VPD values between 0 to 2.8 kPa. Soil evaporation was considered negligible and LE was dominated by the vegetation component, while values for stomatal control were fixed for grasslands [*Mu et al.*, 2007b, Table 1]. Errors were assumed independent between Rsn, Tmin, and Tmax. Owing to the complex model dependence on temperature, error propagation was calculated in steps, where errors were assumed independent between different steps. This assumption of error independence represents a potential source of bias in the analysis,

though several temperature dependencies in the model have low characteristic variability, including air density, surface emissivity and the psychrometric constant.

[30] An estimated 2°C error in RS-ET temperature inputs resulted in a 7.3 W m^{-2} error in model derived LE under the low error scenario, whereas model LE error was 34.9 W m^{-2} under the high error scenario. Rsn error in the low error scenario (50 W m^{-2}) alone resulted in 1.5 W m^{-2} error in LE, whereas model LE error was 17.5 W m^{-2} under the high error scenario (90 W m^{-2}). The sensitivity of the model to error in incoming solar radiation is strongly reduced by surface resistance and therefore the lower bound is below the error sensitivity that would be expected for potential evaporation conditions, where radiation is the primary driver of evaporation. When errors in LE estimates from both Tmin/Tmax and Rsn sources were considered, LE error ranged from 7.4 W m^{-2} (Relative Error RE = 34%) to 38.2 W m^{-2} (RE = 16%) for the low error level scenario for VPD > 0.5 kPa. For the high error level scenario, estimated LE error ranged from 14.9 W m^{-2} (RE = 68%) to 75.1 W m^{-2} (31%) for VPD > 0.5 kPa. Thus meaningful (RE < 100%) LE information can be derived when VPD > 0.04 kPa for
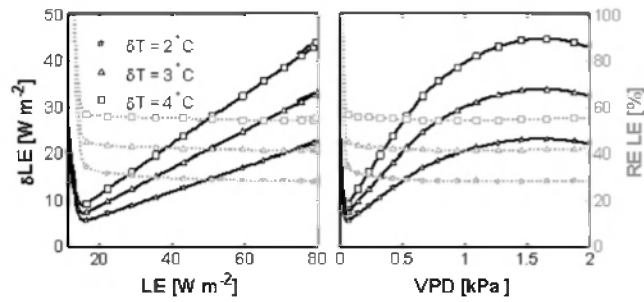
Figure 8. Absolute error (solid black lines; W m^{-2}) and relative error (dashed gray lines; %) propagated to RS-ET estimates of latent energy flux for three levels of error in remotely sensed temperatures. Leaf area index, dew point temperature, net incoming solar radiation, and error in net incoming solar radiation are held at constant, moderate values of 3 m^2 m^{-2}, 0°C, 300 W m^{-2}, and 70 W m^{-2}, respectively. Tmax varies from 0° to 30°C. Soil evaporation is considered negligible.

the low error scenario and when VPD > 0.08 kPa for the high error scenario.

[31] Given a constant error in Tday, the absolute error in LE estimates from Tmin/Tmax and Rsn sources increases linearly with the magnitude of the LE flux when LE is above a threshold of approximately 15 W m^{-2}, while relative LE error is relatively consistent with a small decline (Figure 8). Given a constant error in Tday, the error in LE increases with VPD to a maximum at ≈1.5 kPa and then declines as a result of stress related reductions in canopy conductance (Figure 8). The increasing slope of the saturation vapor pressure curve with temperature also imparts relatively more error to LE for higher temperatures relative to lower temperatures at equivalent VPD. The greatest absolute error in LE therefore occurs when LE is high under high LAI, high Rsn, and low VPD, whereas the greatest relative error occurs when LE is low.

[32] The results of the RS-ET model error analysis indicate that meaningful LE information can be derived given observed accuracies in meteorological drivers when LE > 7–26 W m^{-2} (ET > 0.13–1.33 mm d^{-1}) depending on model and satellite sensor retrieval error. Analytically estimated propagated errors are in accord with errors observed in comparisons with observed data (Figure 6 and section 4.3). Correlation of errors in the real data sets and calculation of model parameters from temperature may increase propagated LE errors above those presented, however correlation between Rsn and air temperatures from independent sources and parameter variability is expected to be low. A 2°C error in temperature inputs influences RS-ET derived ET 2–5 times more than does an error of 50 W m^{-2} in net incoming solar radiation. The accuracy of the meteorological drivers contributes 28 to 65 percent of the overall error in RS-ET estimates of LE and translates to relative error in cumulative ET of approximately 2.8 to 6.5 percent over a 100-day growing season.

[33] The RS-ET algorithm is designed for regular global mapping of ET using satellite remote sensing information from MODIS and GMAO surface meteorology as primary inputs, so the RS-ET model was parameterized using global GMAO data [Zhao et al., 2005; Mu et al., 2007b]. Although

model representation contributes relatively more error to estimated fluxes than the meteorological inputs, relatively improved RS-ET accuracies were obtained using GMAO and AMSR-E inputs in relation to tower meteorological inputs for some sites. Similar results were also obtained from a regional comparison of MODIS (MOD17A2) and tower derived CO_2 (GPP) fluxes across a larger North American network of 15 AmeriFlux sites [Heinsch et al., 2006]. The MODIS MOD17A2 algorithm uses the same GMAO surface meteorology as the RS-ET algorithm. The arithmetic mean difference between GMAO- and tower meteorology–based GPP was 28 (±45) percent, indicating that the GMAO meteorology strongly influences model accuracy and that this influence varies from site to site depending on land cover and climate conditions.

4.4. Implementing the RS-ET Algorithm Over the Pan-Arctic Domain

[34] The mean (2000–2006) annual ET pattern for the pan-Arctic domain as derived from MODIS and GMAO meteorological inputs is presented in Figure 9. The area-weighted average ET in this region was calculated for each MODIS UMD land cover type (Table 4). These results show large ET variability among the regional biomes. The largest annual ET rates occur over forests, while the lowest rates occur over grasslands and shrublands; annual ET rates for savanna and cropland areas are generally intermediate (Figure 9 and Table 4). Ecosystem processes in high-latitude boreal and tundra biomes are strongly constrained by low solar irradiance and freezing temperatures for much of the year so that seasonal patterns in plant photosynthesis (GPP)
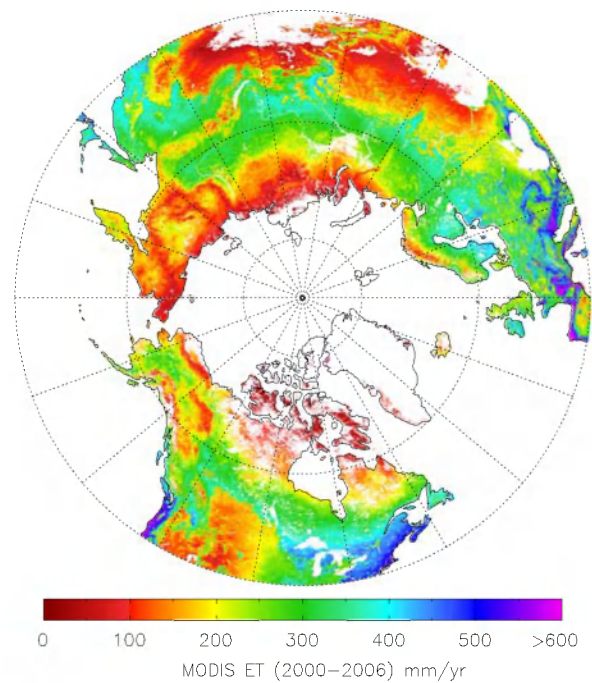
Figure 9. Spatial pattern of model-derived mean annual ET for the pan-Arctic domain obtained using GMAO daily meteorological inputs for the 2000–2006 period. Areas classified by the MODIS global land cover map as open water, ice, and unvegetated are shown in white and were masked from the analysis.

Table 4. Area-Weighted Average Annual ET and the Relative Proportion of the Standard Deviation of Annual Fluxes to Average Annual ET for Each UMD LC in the Pan-Arctic Region Over the 2000–2006 Period[a]

UMD LC	Number	ET (mm yr^{-1})	Standard Deviation to ET (%)
ENF	170283	300	6.60
EBF	2052	596	3.86
DNF	33474	294	6.08
DBF	15592	449	3.80
MF	169445	369	4.49
CSH	330	224	6.46
OSH	323244	163	11.27
WSV	60813	250	7.59
SV	7197	342	4.97
GRS	168485	136	8.45
CRP	256714	256	5.23

[a]ET, evapotranspiration; UMD LC, MODIS land cover class; Number, number of pixels in the pan-Arctic region with that vegetation type; ENF, evergreen needleleaf coniferous forest; EBF, evergreen broadleaf forest; DNF, deciduous needleleaf coniferous forest; DBF, deciduous broadleaf forest; MF, mixed evergreen and deciduous forest; CSH, closed shrublands; OSH, open shrublands; WSV, woody savannas; SV, savanna; GRS, grassland; CRP, cropland.

and ET correspond closely and are generally confined to a relatively narrow growing season [*Jarvis*, 1976; *McMurtrie et al.*, 1992; *Farquhar et al.*, 2002; *Hari et al.*, 1986; *Nemani et al.*, 2003]. As a result, the general spatial patterns of ET (Figure 9) and GPP [*Zhao et al.*, 2005, Figure 7a] are similar within the pan-Arctic domain; forested areas show both high ET and GPP rates, while lower rates occur in grasslands.

[35] Pan-Arctic spatial and seasonal variability was much larger than interannual variability in estimated annual ET; annual ET variability for the 2000–2006 period was generally less than 10% of mean annual ET (Table 4). This relatively low variability reflects the dominance of cold temperature constraints on boreal Arctic ecosystem processes, whereas variability in ecosystem processes and ET is more substantial at lower latitudes and is linked to the increasing importance of plant-available moisture supply [*Nemani et al.*, 2003]. While interannual variability in ET was small, the model results generally showed a large seasonal range of mean monthly ET across the pan-Arctic domain (Figure 10). Mean monthly ET rates increase markedly from winter (DJF) dormancy conditions to spring (MAM) with plentiful solar radiation, seasonal thawing and rising air temperatures and LAI. ET rates are highest in summer (JJA) when seasonal canopy cover indicated by MODIS LAI and EVI inputs is maximized and available solar radiation and seasonal air temperatures are generally optimal for photosynthesis and canopy conductance. Vegetation canopy senescence and decreasing air temperatures and solar energy in the fall (SON) reduce mean monthly ET rates to approximately 81.7% of summer conditions. With predominantly freezing temperatures and near-zero solar irradiance in winter (DJF), plants become dormant and ET is nearly zero.

4.5. Discussion

[36] Results of the model comparisons for the six boreal-Arctic tower sites from this investigation showed no major

differences in modeled ET results produced from the three alternate sets of meteorology inputs despite large spatial and seasonal variability in surface meteorological conditions and estimated ET rates across the pan-Arctic domain and regional tower observation network. The RMSE and mean biases of the GMAO- and AMSR-E-based ET estimates were generally small and corresponded strongly with each other and with associated tower observations. The RS-ET model parameters are the same as those used in the global MODIS primary production algorithm [*Zhao et al.*, 2005]. These parameters have been previously calibrated using GMAO meteorology inputs and a global distribution of tower-based meteorological observations [*Zhao et al.*, 2005; *Mu et al.*, 2007b], which may explain the relatively low mean residual LE error produced from GMAO inputs relative to results from AMSR-E- and tower-based meteorological inputs. The relatively coarse resolution GMAO meteorology also has dampened daily variability as compared to the AMSR-E and tower daily meteorology. However, the lower RMSE values of the AMSR-E-based RS-ET results indicate that the AMSR-E-based daily air temperature and VPD information is generally consistent with tower observations and provides a viable alternative to GMAO meteorological inputs for ET estimation over boreal Arctic regions.

[37] The analysis presented in section 4.1 indicates some model uncertainty due to spatial scale differences between tower observations and GMAO and AMSR-E meteorology inputs. However, point to pixel comparisons between tower observations and model inputs varied by less than 3.40°C for temperature, less than 0.4 kPa for VPD, and less than 88.1 W m^{-2} for radiation. Error in model LE results between the three input meteorology data sets was less
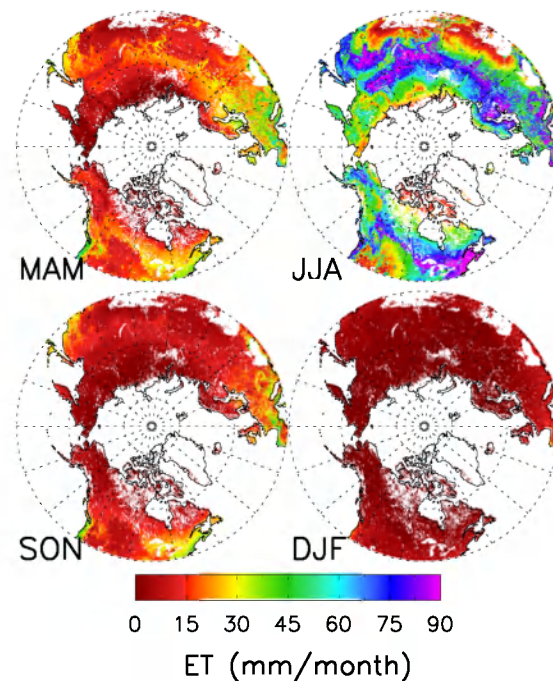
Figure 10. The mean (2000–2006) seasonality of regional ET for the pan-Arctic domain as derived from the RS-ET algorithm and GMAO meteorology. Masked areas are shown in white.

than 8.3 W m^{-2} for all locations, and represented between 2.8–18.3% of the mean RMSE for each location. These results indicate that uncertainties in meteorological inputs have only a minor impact on RS-ET algorithm accuracy for the six boreal Arctic study sites. Tower instrument error and associated data dropout produce differences of approximately 20% when towers are intercalibrated at the same site [*Baldocchi et al.*, 2001; *Baldocchi*, 2003; *Shuttleworth*, 2007]. This indicates potential observational error of 10 to 40 W m^{-2} for yearly average LE fluxes from 50 to 200 W m^{-2}. The remaining model error can be attributed to deviations in algorithm assumptions and MODIS LAI/EVI inputs from local tower conditions.

[38] 1. Input data to the RS-ET algorithm. There are documented biases in model inputs from both GMAO and MODIS data when compared to observations [*Heinsch et al.*, 2006]. Overestimates of LAI by MODIS [*Heinsch et al.*, 2006; *Wang et al.*, 2004] may result in overestimates of LE even if other inputs such as daily meteorology and MODIS EVI data are relatively accurate. Although the temporal filling of unreliable MODIS data, including LAI, EVI and albedo, greatly improves the accuracy of model inputs, the filled values are artificial and therefore contain uncertainties. The RS-ET estimate is very sensitive to fractional vegetation cover, and inaccuracy in MODIS EVI will lead to miscalculation of Fc, and hence LE. By setting Fc to 1.0, the magnitude of LE estimates decreases at the three grass tower sites ATQ, BRW$_1$ and BRW$_2$, but increases at the forest sites NOBS and OAS. LE RMSE and associated model biases increase substantially by setting Fc to 1.0 at these five sites. At LTH, the magnitude of estimated LE increases but is still much lower than tower LE observations; LE RMSE and biases at LTH decrease with Fc = 1, but are still much higher than those at the other five sites with Fc calculated from EVI. All of these input uncertainties can introduce biases in LE (ET) estimates that are difficult to detect.

[39] 2. Missing observation data. To facilitate comparisons between RS-ET results and tower observations, we only analyzed days having complete data series from tower LE observations, and tower, GMAO and AMSR-E derived meteorology inputs. For each tower and each year, there were fewer than 200 days with available data, most of which occurred during the growing seasons. The tower latent heat flux and meteorological data is typically reported at half-hourly intervals. For these available daily observations, there were, on average, fewer than 15 measurements per day. Using so few observation samples to obtain estimates of daily meteorology or a daily average of LE can lead to errors in the analysis [*Desai et al.*, 2005]. However, we chose not to use gap-filled data because gap-filling methods have been tested on net ecosystem exchange of CO$_2$ and not ET, limiting our ability to assess reliability.

[40] 3. Errors in eddy covariance tower LE observations. Two types of towers have been widely employed: Bowen Ratio Energy Balance (BREB) and eddy covariance (EC) towers. Flux measurements are subject to several sources of error [*Glenn et al.*, 2008]. They are point measurements, but they require a uniform fetch of vegetation of several thousand square meters (e.g., 50 m × 50 m) around the towers to produce results that are representative of a particular ecosystem, and these conditions are often not perfectly met in natural landscapes. Instrument error and data dropout introduce errors of about 20% when different towers are intercalibrated at the same site [*Baldocchi et al.*, 2001; *Baldocchi*, 2003; *Shuttleworth*, 2007]. Furthermore, EC moisture flux estimates are often 10–30% lower than energy closure (BREB) results. EC results are often increased to account for this "closure error" [*Twine et al.*, 2000], but the best way to achieve closure and the cause of the closure error are still unclear [*Shuttleworth*, 2007]. LE observations from eddy covariance may therefore be biased as a result of energy balance closure error.

[41] 4. Scaling from tower to landscape. The size of the flux tower footprint is largely influenced by tower height and local environmental conditions [*Cohen et al.*, 2003; *Turner et al.*, 2003a, 2003b]. The RS-ET input data are representative of different spatial resolutions which may introduce uncertainties across the six study sites due to differences in tower footprints for different towers and under varying environmental conditions for a given tower. The GMAO meteorology at 1 × 1.25 degree and the 60 km × 60 km AMSR-E meteorology are much coarser than the 1-km MODIS EVI and LAI input data. Previous modeling studies of land cover spatial scale effects on estimated ET fluxes indicate that ET is relatively insensitive to land cover spatial scale in relatively moist boreal environments, with an average bias of less than 5% between regional model estimates consistent with satellite observations and tower observed fluxes [*Kimball and Running*, 1999].

[42] 5. Algorithm limitations. Model assumptions contribute to the observed differences between RS-ET and tower observed fluxes. First, the RS-ET algorithm assumes that net incoming radiation and VPD are negligible at night (day length is calculated in the RS-ET model, which can be 24 h long in summer in the polar arctic), which results in no estimated nighttime LE flux. However, outgoing longwave radiation is not negligible at night, and nighttime air temperatures may not attain saturation (i.e., nonnegligible VPD). The assumption of a negligible ground heat flux (G) on a daily basis [*Gavilána et al.*, 2007] may cause some errors in the Arctic boreal regions, where G accounts for 10–15% of net solar radiation for melting ice in the active layer, especially early in the growing season [*Harazono et al.*, 1995; *Engstrom et al.*, 2006]. In the Arctic boreal regions, the observed G at four of the six studied towers shows that, for most of the time especially in summer, G counts to less than 20% of the net incoming solar radiation (not shown). *Jacobsen and Hansen* [1996] have established some methods to estimate G using the surface temperature or some vegetation index. In our future improvements, we will refer to their method to estimate the ground heat fluxes to make the ET estimates more accurate. MODIS ET algorithm was developed to estimate global ET. It remains a significant challenge to estimate the ground heat flux at different climate regimes and vegetation types. The potential stomatal conductance per unit leaf area (c_L in equation (A2)) was taken as a constant. It actually varies with different vegetation types. *Leuning et al.* [2008] indicate that this key parameter in the Penman-Monteith equation varies clearly in the fifteen global ecosystems. Another limitation of this algorithm is that it does not consider water balance constrains, resulting in significant errors in mean annual remote

sense evaporation in semiarid and arid regions [*Zhang et al.*, 2008], e.g., mean annual remotely sensed evaporation higher than mean annual rainfall. The limitations of these assumptions will introduce biases and errors in the ET estimates. Future improvements in the RS-ET model should consider biome-specific variability in ground heat flux. Also model biophysical parameters, such as the critical VPD values when stomata are completely inhibited (VPD_close) or under no water stress (VPD_open) are used as constant parameters within a given biome type as defined from a global land cover classification. However, for different species within the same biome type, the differences in these parameters can be large [*Turner et al.*, 2003a, 2003b]. In addition, the RS-ET model treats nonvegetated areas as a uniform evaporating surface. For example, the BRW and ATQ sites contained 87% and 12% respective open water coverage [*Jones*, 2007]. The large ocean component at the BRW and ATQ site windows reduced vegetation fractional cover derived from the EVI [*Mu et al.*, 2007b], making surface evaporation the primary component of estimated ET. Consequently, plant transpiration is only a small part of estimated ET for the BRW and ATQ sites. The ocean and other open water bodies are also treated as a soil surface by the model, even though evaporation over water is characteristically much higher than over soil. As a result, model ET rates are generally smaller than tower observations for the BRW and ATQ sites (Table 3). Further study is needed to improve RS-ET algorithm performance particularly where vegetation cover is less extensive and evaporation from open water and other nonvegetated surfaces represents a larger component of ET.

5. Conclusion

[43] The satellite-based RS-ET algorithm produced large spatial and seasonal variability in annual ET rates corresponding with regional land cover and strong seasonality in available solar radiation, temperature and plant growth. Spatial variability in model derived annual ET was generally consistent with satellite-based regional productivity (GPP) patterns and showed relatively small variability in annual ET over the 2000–2006 study period; this was attributed to strong cold temperature constraints on ecosystem processes, relatively short growing seasons and large seasonal ranges in solar radiation, vegetation canopy and temperature conditions regulating land-atmosphere water and trace gas exchange for the domain. The RS-ET model results derived from the three alternate meteorology data sets agreed well with tower observed latent heat fluxes (r > 0.7; P < 0.003; RMSE < 30 W m^{-2}) and captured regional ET patterns and daily, seasonal and interannual variability in ET across the six tower sites representing relatively diverse boreal Arctic land cover and climate conditions. The MODIS-AMSR-E derived ET results also showed comparable accuracy to ET results derived from GMAO reanalysis meteorology, while ET estimation error was generally more a function of algorithm parameterization than differences in meteorology drivers. Uncertainty in daily meteorological inputs contributed from 28 to 65 percent of the overall error in RS-ET estimates of LE and corresponds to relative error in cumulative ET of approximately 2.8 to 6.5 percent over a 100-day growing season. These results are within the range of accuracy for tower-based ET

measurements and indicate significant potential for regional mapping and monitoring of daily land surface evaporation using synergistic information from satellite optical IR and microwave remote sensing.

Appendix A: ET Algorithm Logic

[44] The RS-ET was developed to estimate global ET by considering both the surface energy partitioning process and environmental constraints on ET based on *Cleugh et al.*'s [2007] Penman-Monteith-based ET:

$$\lambda E = \frac{sA + \rho Cp(e_{sat} - e)/r_a}{s + \gamma(1 + r_s/r_a)} \tag{A1}$$

where λE (W m^{-2}) is the latent heat flux and λ (J kg^{-1}) is the latent heat of evaporation; $s = d(esat)/dT$ (Pa K^{-1}) and is the slope of the curve relating saturated water vapor pressure (*esat*: Pa) to temperature; A (W m^{-2}) is available energy; ρ (Kg m^{-3}) is air density; C_p (J kg^{-1} K^{-1}) is the specific heat capacity of air; e (Pa) is the actual water vapor pressure; and r_a (s m^{-1}) is the aerodynamic resistance. The psychrometric constant γ (Pa K^{-1}) is given by $\gamma = (M_a/M_w)(C_pP/\lambda)$, where M_a (kg mol^{-1}) and M_w (kg mol^{-1}) are the molecular masses of dry air and wet air, respectively, and P (Pa) is atmospheric pressure [*Maidment*, 1993]. Surface resistance (r_s: s m^{-1}) is an effective resistance to evaporation from the soil surface and transpiration from the plant canopy. Input data to the algorithm include daily meteorology (temperature, actual vapor pressure, and incoming solar radiation) and remotely sensed LAI and NDVI. In addition, this algorithm is computed daily to take advantage of widely available daily meteorology, overcoming the obstacle of using the 8-day MODIS LST data.

A1. Calculation of Canopy Conductance

[45] In RS-ET, surface conductance (C_C) is estimated by using LAI as a scalar to convert the stomatal conductance (*Cs*) calculated at the leaf level to a canopy conductance (*Cc*) [*Landsberg and Gower*, 1997]:

$$\begin{aligned} C_S &= c_L \times m(T\min) \times m(VPD) \\ Cc &= Cs \times LAI \end{aligned} \tag{A2}$$

where c_L is the mean potential stomatal conductance per unit leaf area, $m(T\min)$ is a multiplier that limits potential stomatal conductance by minimum air temperatures ($T\min$), and $m(VPD)$ is a multiplier used to reduce the potential stomatal conductance when VPD is high enough to inhibit photosynthesis. In the case of plant transpiration, surface conductance (g_s) is equal to the canopy conductance, and hence surface resistance (r_s) is the inverse of canopy conductance (C_C). The LAI in equation (A2) is obtained from the global 8-day standard MODIS LAI product, which is estimated using a canopy radiation transfer model combined with remotely sensed surface reflectance data [*Myneni et al.*, 2002].

A2. Calculation of Vegetation Cover Fraction

[46] Vegetation cover fraction (F_C) is defined as the fraction of ground surface covered by the maximum extent of the vegetation canopy (varies between 0 and 1). In the

RS-ET algorithm, vegetation cover fraction is calculated by using EVI as

$$F_C = \frac{EVI - EVI_{\min}}{EVI_{\max} - EVI_{\min}} \qquad (A3)$$

where $EVI_{\min}$ and $EVI_{\max}$ are the signals from bare soil (LAI $\rightarrow$ 0) and dense green vegetation (LAI $\rightarrow \infty$) [*Gutman and Ignatov*, 1998], which are set as seasonally and geographically invariant constants 0.05 and 0.95, respectively. When Fc is bigger than 1, Fc is 1, and when Fc is less than 0, Fc is 0. We have done several sensitivity experiments, setting ($EVI_{\min}$, $EVI_{\max}$) as (0.01, 0.99), (0.05, 0.92), (0.11, 0.92) and (−0.5, 0.99), respectively. There is not much difference between the root mean square error (less than 1.0 W m^{-22}), bias (about 3.0 W m^{-22}) and correlation coefficient (less than 0.01) from different sensitivity experiments.

[47] Net radiation is linearly partitioned between the canopy and the soil surface using this vegetation cover fraction (F_C) such that

$$\begin{aligned} A_C &= F_C \times A \\ A_{SOIL} &= (1 - F_C) \times A \end{aligned} \qquad (A4)$$

where A_C and A_{SOIL} are the total net incoming radiation (A) partitioned to the canopy and soil, respectively.

A3. Soil Evaporation

[48] To calculate soil evaporation, the potential evaporation (λE_{SOIL_POT}) is first calculated using the Penman-Monteith equation (equation (A1)). The total aerodynamic resistance to vapor transport (r_{tot}) is the sum of surface resistance (r_s) and the aerodynamic resistance for vapor transport (r_v) such that $r_{tot} = r_v + r_s$ [*van de Griend*, 1994]. A constant r_{totc} (107 s m^{-1}) for r_{tot} is assumed globally on the basis of observations of the ground surface in tiger-bush in southwest Niger [*Wallace and Holwill*, 1997], but it is corrected (rcorr) for atmospheric temperature (T) and pressure (P) [*Jones*, 1992] with standard conditions assumed to be T = 20°C and P = 101300 Pa:

$$rcorr = \frac{1.0}{\left(\dfrac{273.15 + T}{293.15}\right)^{1.75} \times \dfrac{101300}{Pa}}$$

$$r_{tot} = r_{totc} \times rcorr = r_v + r_s \qquad (A5)$$

$$r_{totc} = 107.0$$

[49] We assume that r_v (s m^{-1}) is equal to the aerodynamic resistance (r_a: s m^{-1}) from equation (A1) since the values of r_v and r_a are usually very close [*van de Griend*, 1994]. The aerodynamic resistance (r_a) is parallel to both the resistance to convective heat transfer (r_c: s m^{-1}) and the resistance to radiative heat transfer (r_r: s m^{-1}) [*Choudhury and DiGirolamo*, 1998], such that

$$r_r = \frac{\rho \times C_P}{4.0 \times \sigma \times T^3}$$

$$r_a = \frac{r_c \times r_r}{r_c + r_r} \qquad (A6)$$

The r_c is assumed to be equal to boundary layer resistance, which is calculated in the same way as total aerodynamic resistance (r_{tot}) from equation (A5) [*Thornton*, 1998]. Finally, the actual soil evaporation (λE_{SOIL}) is calculated in equation (A5) using potential soil evaporation (λE_{SOIL_POT}) and the complementary relationship hypothesis [*Bouchet*, 1963; *Fisher et al.*, 2008], which defines land-atmosphere interactions from vapor pressure deficit and relative humidity (RH, %):

$$\begin{aligned} \lambda E_{SOIL\_POT} &= \frac{sA_{SOIL} + \rho Cp(e_{sat} - e)/r_a}{s + \gamma \times \left(1 + \dfrac{r_s}{r_a}\right)} \\ &= \frac{sA_{SOIL} + \rho Cp(e_{sat} - e)/r_a}{s + \gamma \times \dfrac{r_{tot}}{r_a}} \end{aligned} \qquad (A7)$$

$$\lambda E_{SOIL} = \lambda E_{SOIL\_POT} \times \left(\frac{RH}{100}\right)^{(esat-e)/100}$$

[50] The value of 50 s m^{-1} was chosen as the lower bound because it is very close to the mean boundary layer resistance for vegetation under semiarid conditions, and there is little variation around this mean [*van de Griend*, 1994]. Finally, the latent heat flux for the ecosystem is calculated as the sum of the transpiration (equation (A1)) and the soil evaporation (equation (A7)).

References

Ashcroft, P., and F. Wentz (1999), Algorithm theoretical basis document, AMSR level 2A algorithm, *Tech. Rep. 121599B–1*, Remote Sens. Syst., Santa Rosa, Calif.

Baldocchi, D. (2003), Assessing the eddy covariance technique for evaluating carbon dioxide exchange rates of ecosystems: Past, present and future, *Global Change Biol.*, 9, 479–492, doi:10.1046/j.1365-2486.2003.00629.x.

Baldocchi, D. (2008), 'Breathing' of the terrestrial biosphere: Lessons learned from a global network of carbon dioxide flux measurement systems, *Aust. J. Bot.*, 56, 1–26, doi:10.1071/BT07151.

Baldocchi, D., et al. (2001), Fluxnet: A new tool to study the temporal and spatial variability of ecosystem-scale carbon dioxide, water vapor, and energy flux densities, *Bull. Am. Meteorol. Soc.*, 82, 2415–2434.

Bastiaanssen, W. G. M., M. Menenti, R. A. Feddes, and A. A. M. Holtslag (1998a), A remote sensing surface energy balance algorithm for land (SEBAL): 1. Formulation, *J. Hydrol.*, 212–213, 198–212.

Bastiaanssen, W. G. M., M. Menenti, R. A. Feddes, and A. A. M. Holtslag (1998b), The surface energy balance algorithm for land (SEBAL): 2. Validation, *J. Hydrol.*, 212–213, 213–229, doi:10.1016/S0022-1694(98)00254-6.

Bouchet, R. J. (1963), Evapotranspiration re'elle evapotranspiration potentielle, signification climatique, *Int. Assoc. Sci. Hydrol. Publ.*, 62, 134–142.

Chanzy, A., and W. P. Kustas (1994), Evaporation monitoring over land surface using microwave radiometry, in *Passive Microwave Remote Sen-*

sing of Land-Atmosphere Interactions, edited by B. J. Choudbury et al., pp. 531–550, VSP, Utrecht, Netherlands.

Choudhury, B. J., and N. E. DiGirolamo (1998), A biophysical process-based estimate of global land surface evaporation using satellite and ancillary data I. Model description and comparison with observations, *J. Hydrol.*, 205, 164–185, doi:10.1016/S0022-1694(97)00147-9.

Cleugh, H. A., R. Leuning, Q. Mu, and S. W. Running (2007), Regional evaporation estimates from flux tower and MODIS satellite data, *Remote Sens. Environ.*, 106, 285–304, doi:10.1016/j.rse.2006.07.007.

Cohen, W. B., T. K. Maiersperger, Z. Yang, S. T. Gower, D. P. Turner, W. D. Ritts, M. Berterretche, and S. W. Running (2003), Comparisons of land cover and LAI estimates derived from ETM+ and MODIS for four sites in North America: A quality assessment of 2000/2001 provisional MODIS products, *Remote Sens. Environ.*, 88, 233–255, doi:10.1016/j.rse.2003.06.006.

Dang, Q. L., H. A. Margolis, M. R. Coyea, M. Sy, and G. J. Collatz (1997), Regulation of branch-level gas exchange of boreal trees: Roles of shoot water potential and vapour pressure difference, *Tree Physiol.*, 17, 521–535.

Desai, A. R., P. V. Bolstad, B. D. Cook, K. J. Davis, and E. V. Carey (2005), Comparing net ecosystem exchange of carbon dioxide between an old-growth and mature forest in the upper midwest, USA, *Agric. For. Meteorol.*, 128, 33–55, doi:10.1016/j.agrformet.2004.09.005.

Donohue, R. J., M. L. Roderick, and T. R. McVicar (2007), On the importance of including vegetation dynamics in Budyko's hydrological model, *Hydrol. Earth Syst. Sci.*, 11, 983–995.

Dunn, A. L. (2006), Carbon fluxes and the boreal forest mosaic, Ph.D. dissertation, Dep. of Earth and Planet. Sci., Harvard Univ., Cambridge, Mass.

Engstrom, R., A. Hope, H. Kwon, Y. Harazono, M. Mano, and W. Oechel (2006), Modeling evapotranspiration in Arctic coastal plain ecosystems using a modified BIOME-BGC model, *J. Geophys. Res.*, 111, G02021, doi:10.1029/2005JG000102.

Farquhar, G. D., T. N. Buckley, and J. M. Miller (2002), Optimal stomatal control in relation to leaf area and nitrogen content, *Silva Fennica*, 36(3), 625–637.

Fetzer, E., et al. (2003), AIRS/AMSU/HSB validation, *IEEE Trans. Geosci. Remote Sens.*, 41(2), 418–431, doi:10.1109/TGRS.2002.808293.

Fily, M., A. Royer, K. Goita, and C. Prigent (2003), A simple retrieval method for land surface temperature and fraction of water surface determination from satellite microwave brightness temperatures in sub-Arctic areas, *Remote Sens. Environ.*, 85, 328–338, doi:10.1016/S0034-4257(03)00011-7.

Fisher, J. B., K. P. Tu, and D. D. Baldocchi (2008), Global estimates of the land-atmosphere water flux based on monthly AVHRR and ISLSCP-II data, validated at 16 FLUXNET sites, *Remote Sens. Environ.*, 112, 901–919, doi:10.1016/j.rse.2007.06.025.

Friedl, M. A. (1996), Relationships among remotely sensed data, surface energy balance, and area-averaged fluxes over partially vegetated land surfaces, *J. Appl. Meteorol.*, 35, 2091–2103, doi:10.1175/1520-0450(1996)035<2091:RARSDS>2.0.CO;2.

Gash, J. H. C. (1987), An analytical framework for extrapolating evaporation measurements by remote sensing surface temperature, *Int. J. Remote Sens.*, 8, 1245–1249, doi:10.1080/01431168708954769.

Gavilána, P., J. Berengenaa, and R. G. Allen (2007), Measuring versus estimating net radiation and soil heat flux: Impact on Penman–Monteith reference ET estimates in semiarid regions, *Agric. Water Manage.*, 89(3), 275–286.

Glenn, E. P., A. R. Huete, P. L. Nagler, and S. G. Nelson (2008), Relationship between remotely sensed vegetation indices, canopy attributes, and plant physiological processes: What vegetation indices can and cannot tell us about the landscape, *Sensors*, 8, 2136–2160.

Granger, R. J., and D. M. Gray (1989), Evaporation from natural nonsaturated surfaces, *J. Hydrol.*, 111, 21–29, doi:10.1016/0022-1694(89)90249-7.

Griffis, J., T. A. Black, D. Gaumont-Guay, G. B. Drewitt, Z. Nesic, A. G. Barr, K. Morgenstem, and N. Kljun (2004), Seasonal variation and partitioning of ecosystem respiration in a southern boreal aspen forest, *Agric. For. Meteorol.*, 125, 207–223, doi:10.1016/j.agrformet.2004.04.006.

Gutman, G., and A. Ignatov (1998), Derivation of green vegetation fraction from NOAA/AVHRR for use in numerical weather prediction models, *Int. J. Remote Sens.*, 19, 1533–1543, doi:10.1080/014311698215333.

Harazono, Y., M. Yoshimoto, A. Miyata, Y. Uchida, G. L. Vourlitis, and W. C. Oechel (1995), Micrometeorological data and their characteristics over the Arctic tundra at Barrow, Alaska during the summer of 1993, *Misc. Publ. Natl. Inst. Agro-Environ. Sci.*, 16, 1–213.

Harazono, Y., M. Mano, A. Miyata, R. C. Zulueta, and W. C. Oechel (2003), Inter-annual carbon uptake of a wet sedge tundra ecosystem in the Arctic, *Tellus B*, 55, 215–231.

Hari, P., A. Makela, E. Korpilahti, and M. Holmberg (1986), Optimal control of gas exchange, *Tree Physiol.*, 2, 169–175.

Hashimoto, H., J. L. Dungan, M. A. White, F. Yang, A. R. Michaelis, S. W. Running, and R. R. Nemani (2008), Satellite-based estimation of surface vapor pressure deficits using MODIS land surface temperature data, *Remote Sens. Environ.*, 112, 142–155, doi:10.1016/j.rse.2007.04.016.

Heinsch, F. A., et al. (2006), Evaluation of remote sensing based terrestrial productivity from MODIS using AmeriFlux tower eddy flux network observations, *IEEE Trans. Geosci. Remote Sens.*, 44, 1908–1925, doi:10.1109/TGRS.2005.853936.

Hinkel, K. M., W. R. Eisner, J. G. Bockheim, F. E. Nelson, K. M. Peterson, and X. Dai (2003), Spatial extent, age, and carbon stocks in drained thaw lake basins on the Barrow Peninsula, Alaska, *Arct. Antarct. Alp. Res.*, 35(3), 291–300, doi:10.1657/1523-0430(2003)035[0291:SEAACS]2.0.CO;2.

Huete, A., K. Didan, T. Miura, E. P. Rodriguez, X. Gao, and L. G. Ferreira (2002), Overview of the radiometric and biophysical performance of the MODIS vegetation indices, *Remote Sens. Environ.*, 83, 195–213, doi:10.1016/S0034-4257(02)00096-2.

Huete, A. R., K. Didan, Y. E. Shimabukuro, P. Ratana, S. R. Saleska, L. R. Hutyra, W. Yang, R. R. Nemani, and R. Myneni (2006), Amazon rainforests green-up with sunlight in dry season, *Geophys. Res. Lett.*, 33, L06405, doi:10.1029/2005GL025583.

Jacobsen, A., and B. U. Hansen (1996), Estimation of the soil heat flux/net radiation ratio over high-latitude natural vegetation using spectral vegetation indices, in *4th Circumpolar Symposium on Remote Sensing of the Polar Environments: Lyngby, Denmark 29 April–1 May 1996*, edited by T.-D. Guyenne, *ESA SP-391*, 33–38.

Janowiak, J. E., A. Gruber, C. R. Kondragunta, R. E. Livezey, and G. J. Huffman (1998), A Comparison of the NCEP–NCAR Reanalysis Precipitation and the GPCP Rain Gauge–Satellite Combined Dataset with Observational Error Considerations, *J. Clim.*, 11, 2960–2979.

Jarvis, P. G. (1976), The interpretation of the variations in leaf water potential and stomatal conductance found in canopies in the field, *Philos. Trans. R. Soc. London, Ser. B*, 273, 593–610, doi:10.1098/rstb.1976.0035.

Jones, H. G. (1992), *Plants and Microclimate: A Quantitative Approach to Environmental Plant Physiology*, Cambridge Univ. Press, Cambridge, U. K.

Jones, L. A. (2007), Satellite microwave remote sensing of Boreal-Arctic land surface state and meteorology from AMSR-E, M.S. thesis, Univ. of Montana, Missoula, Mont.

Jones, L. A., J. S. Kimball, K. C. McDonald, S. T. K. Chan, E. Njoku, and W. C. Oechel (2007), Satellite microwave remote sensing of boreal and Arctic soil temperatures from AMSR-E, *IEEE Trans. Geosci. Remote Sens.*, 45, 2004–2018, doi:10.1109/TGRS.2007.898436.

Justice, C. O., J. R. G. Townshend, E. F. Vermote, E. Masuoka, R. E. Wolfe, N. Saleous, D. P. Roy, and J. T. Morisette (2002), An overview of MODIS land data processing and product status, *Remote Sens. Environ.*, 83, 3–15, doi:10.1016/S0034-4257(02)00084-6.

Kalma, J. D., and D. L. B. Jupp (1990), Estimating evaporation from pasture using infrared thermometry: Evaluation of a one-layer resistance model, *Agric. For. Meteorol.*, 51, 223–246, doi:10.1016/0168-1923(90)90110-R.

Kimball, J. S., and S. W. Running (1999), Sensitivity of boreal forest regional water flux and net primary production simulations to sub-grid-scale land cover complexity, *J. Geophys. Res.*, 104, 27,789–27,801, doi:10.1029/1999JD900085.

Kimball, J. S., S. W. Running, and R. Nemani (1997), An improved method for estimating surface humidity from daily minimum temperature, *Agric. For. Meteorol.*, 85, 87–98, doi:10.1016/S0168-1923(96)02366-0.

Kimball, J. S., M. Zhao, K. C. McDonald, and S. W. Running (2006), Satellite remote sensing of terrestrial net primary production for the pan-Arctic basin and Alaska, *Mitigation Adaptation Strategies Global Change*, 11, 783–804, doi:10.1007/s11027-005-9014-5.

Korzoun, V. I., et al. (1978), *Atlas of World Water Balance*, U. N. Educ. Sci. Cult. Organ., Paris.

Landsberg, J. J., and S. T. Gower (1997), *Applications of Physiological Ecology to Forest Management*, Academic, San Diego, Calif.

Leuning, R., Y. Q. Zhang, A. Rajaud, H. Cleugh, and K. Tu (2008), A simple surface conductance model to estimate regional evaporation using MODIS leaf area index and the Penman-Monteith equation, *Water Resour. Res.*, 44, W10419, doi:10.1029/2007WR006562.

Los, S. O., G. J. Collatz, P. J. Sellers, C. M. Malmstrom, N. H. Pollack, R. S. DeFries, L. Bounoua, M. T. Parris, C. J. Tucker, and D. A. Dazlich (2000), A global 9-yr biophysical land surface dataset from NOAA AVHRR data, *J. Hydrometeorol.*, *1*(2), 183–199, doi:10.1175/1525-7541(2000)001<0183:AGYBLS>2.0.CO;2.

Lucht, W., C. B. Schaaf, and A. H. Strahler (2000), An algorithm for the retrieval of albedo from space using semiempirical BRDF models, *IEEE Trans. Geosci. Remote Sens.*, *38*, 977–998, doi:10.1109/36.841980.

L'vovich, M. I., and G. F. White (1990), Use and transformation of terrestrial water systems, in *The Earth as Transformed by Human Action*, edited by B. L. Turner II et al., pp. 235–252, Cambridge Univ. Press, New York.

Maddock, T., III, et al. (1998), An overview of atmospheric and surface water coupling to regional groundwater models in semi-arid basins, paper presented at Special Symposium on Hydrology, Am. Soc. of Meteorol., Phoenix, Ariz., 11–16 Jan.

Maidment, D. R. (Ed.) (1993), *Handbook of Hydrology*, McGraw Hill, New York.

Marsden, B. J., V. J. Lieffers, and J. J. Zwiazek (1996), The effect of humidity on photosynthesis and water relations of white spruce seedlings during the early establishment phase, *Can. J. For. Res.*, *26*, 1015–1021, doi:10.1139/x26-112.

McGuire, A. D., et al. (2008), The Western Arctic Linkage Experiment (WALE): Overview and synthesis, *Earth Interact.*, *12*, 1–13.

McMurtrie, R. E., R. Leuning, W. A. Thompson, and A. M. Wheeler (1992), A model of canopy photosynthesis and water use incorporating a mechanistic formulation of leaf CO_2 exchange, *For. Ecol. Manage.*, *52*, 261–278, doi:10.1016/0378-1127(92)90505-4.

McVicar, T. R., T. G. Van Niel, L. T. Li, M. F. Hutchinson, X. M. Mu, and Z. H. Liu (2007), Spatially distributing monthly reference evapotranspiration and pan evaporation considering topographic influences, *J. Hydrol.*, *338*, 196–220.

Misson, L., J. A. Panek, and A. H. Goldstein (2004), A comparison of three approaches to modeling leaf gas exchange in annually drought-stressed ponderosa pine forests, *Tree Physiol.*, *24*, 529–541.

Monteith, J. L. (1964), Evaporation and environment, in *The State and Movement of Water in Living Organisms, Symp. Soc. Exp. Biol.*, vol. 19, pp. , 205–234Cambridge Univ. Press, Cambridge, U. K.

Morton, F. I. (1983), Operational estimates of areal evapotranspiration and their significance to the science and pratice of hydrology, *J. Hydrol.*, *66*, 1–76, doi:10.1016/0022-1694(83)90177-4.

Mu, Q., M. Zhao, F. A. Heinsch, M. Liu, H. Tian, and S. W. Running (2007a), Evaluating water stress controls on primary production in biogeochemical and remote sensing based models, *J. Geophys. Res.*, *112*, G01012, doi:10.1029/2006JG000179.

Mu, Q., F. A. Heinsch, M. Zhao, and S. W. Running (2007b), Development of a global evapotranspiration algorithm based on MODIS and global meteorology data, *Remote Sens. Environ.*, *111*, 519–536, doi:10.1016/j.rse.2007.04.015.

Myneni, R. B., et al. (2002), Global products of vegetation leaf area and fraction absorbed PAR from year one of MODIS data, *Remote Sens. Environ.*, *83*, 214–231, doi:10.1016/S0034-4257(02)00074-3.

Neilson, R. P. (1995), A model for predicting continental-scale vegetation distribution and water balance, *Ecol. Appl.*, *5*, 362–385.

Nemani, R. R., C. D. Keeling, H. Hashimoto, W. M. Jolly, S. C. Piper, C. J. Tucker, R. B. Myneni, and S. W. Running (2003), Climate-driven increases in global terrestrial net primary production from 1982 to 1999, *Science*, *300*, 1560–1563, doi:10.1126/science.1082750.

Oak Ridge National Laboratory Distributed Active Archive Center (2006), MODIS subsetted land products, Collection 4, 12 June, http://www.daac.ornl.gov/MODIS/modis.html, Oak Ridge, Tenn.

Oechel, W. C., G. L. Vourlitis, S. J. Hastings, R. P. Ault Jr., and P. Bryant (1998), The effects of water table manipulation and elevated temperature on the net CO_2 flux of wet sedge tundra ecosystems, *Global Change Biol.*, *4*, 77–90, doi:10.1046/j.1365-2486.1998.00110.x.

Oechel, W. C., G. L. Vourlities, S. J. Hastings, R. M. Zulueta, L. D. Hinzman, and D. L. Kane (2000), Acclimation of ecosystem CO_2 exchange in the Alaskan Arctic in response to decadal climatic warming, *Nature*, *406*, 978–981, doi:10.1038/35023137.

Oren, R., J. S. Perry, G. G. Katul, D. E. Pataki, B. E. Ewers, N. Phillips, and K. V. R. Schäfer (1999), Survey and synthesis of intra- and interspecific variation in stomatal sensitivity to vapour pressure deficit, *Plant Cell Environ.*, *22*, 1515–1526, doi:10.1046/j.1365-3040.1999.00513.x.

Prentice, I. C., W. Cramer, S. P. Harrison, R. Leemans, R. A. Monserud, and A. M. Solomon (1992), A global biome model based on plant physiology and dominance, soil properties and climate, *J. Biogeogr.*, *19*, 117–134.

Priestley, C. H. B., and R. J. Taylor (1972), On the assesment of surface heat flux and evaporation using large scale parameters, *Mon. Weather Rev.*, *100*, 81–92, doi:10.1175/1520-0493(1972)100<0081:OTAOSH>2.3.CO;2.

Pulliainen, J. T., J. Grandell, and M. T. Hallikainen (1997), Retrieval of surface temperature in boreal forest zone from SSM/I data, *IEEE Trans. Geosci. Remote Sens.*, *35*, 1188–1200, doi:10.1109/36.628786.

Raich, J. W., E. B. Rastetter, J. M. Melillo, D. W. Kicklighter, P. A. Steudler, B. J. Peterson, A. L. Grace, B. Moore III, and C. J. Vörösmarty (1991), Potential net primary productivity in South America: Application of a global model, *Ecol. Appl.*, *1*, 399–429, doi:10.2307/1941899.

Rana, G., and N. Katerji (2000), Measurement and estimation of actual evapotranspiration in the field under Mediterranean climate: A review, *Eur. J. Agron.*, *13*, 125–153, doi:10.1016/S1161-0301(00)00070-8.

Running, S. W., and R. R. Nemani (1988), Relating seasonal patterns of the AVHRR vegetation index to simulate photosynthesis and transpiration of forests in different climates, *Remote Sens. Environ.*, *24*, 347–367, doi:10.1016/0034-4257(88)90034-X.

Running, S. W., R. R. Nemani, F. A. Heinsch, M. Zhao, M. C. Reeves, and H. Hashimoto (2004), A continuous satellite-derived measure of global terrestrial primary production, *BioScience*, *54*, 547–560, doi:10.1641/0006-3568(2004)054[0547:ACSMOG]2.0.CO;2.

Schaaf, C. B., et al. (2002), First operational BRDF, albedo and nadir reflectance products from MODIS, *Remote Sens. Environ.*, *83*, 135–148, doi:10.1016/S0034-4257(02)00091-3.

Sellers, P. J., et al. (1996), Comparison of radiative and physiological effects of doubled atmospheric CO_2 on climate, *Science*, *271*, 1402–1406, doi:10.1126/science.271.5254.1402.

Shuttleworth, W. (2007), Putting the 'vap' in evaporation, *Hydrol. Earth Syst. Sci.*, *11*, 210–244.

Su, Z. (2002), The surface energy balance system (SEBS) for estimation of turbulent heat fluxes, *Hydrol. Earth Syst. Sci.*, *6*, 85–99.

Thornton, P. E. (1998), Regional ecosystem simulation: Combining surface- and satellite-based observations to study linkages between terrestrial energy and mass budgets, Ph.D. dissertation, 280 pp., Sch. of For. Univ. of Montana, Missoula, Mont.

Turner, D. P., S. Urbanski, D. Bremer, S. C. Wofsy, T. Meyers, S. T. Gower, and M. Gregory (2003a), A cross-biome comparison of daily light use efficiency for gross primary production, *Global Change Biol.*, *9*, 383–395, doi:10.1046/j.1365-2486.2003.00573.x.

Turner, D. P., W. D. Ritts, W. B. Cohen, S. T. Gower, M. Zhao, S. W. Running, S. C. Wofsy, S. Urbanski, A. L. Dunn, and J. W. Munger (2003b), Scaling gross primary production (GPP) over boreal and deciduous forest landscapes in support of MODIS GPP product validation, *Remote Sens. Environ.*, *88*, 256–270, doi:10.1016/j.rse.2003.06.005.

Twine, T., W. Kustas, J. Norman, D. Cook, P. Houser, T. Meyers, J. Prueger, P. Starks, and M. Wesely (2000), Correcting eddy-covariance flux underestimates over a grassland, *Agric. For. Meteorol.*, *103*, 279–300, doi:10.1016/S0168-1923(00)00123-4.

van de Griend, A. A. (1994), Bare soil surface resistance to evaporation by vapor diffusion under semiarid conditions, *Water Resour. Res.*, *30*, 181–188, doi:10.1029/93WR02747.

Vörösmarty, C. J., C. A. Federer, and A. L. Schloss (1998), Potential evaporation function compared on US watersheds: Possible implication for global-scale water balance and terrestrial ecosystem, *J. Hydrol.*, *207*, 147–169, doi:10.1016/S0022-1694(98)00109-7.

Wallace, J. S., and C. J. Holwill (1997), Soil evaporation from tiger-bush in south-west Niger, *J. Hydrol.*, *188–189*, 426–442, doi:10.1016/S0022-1694(96)03185-X.

Wang, Y., et al. (2004), Evaluation of the MODIS LAI algorithm at a coniferous forest site in Finland, *Remote Sens. Environ.*, *91*, 114–127, doi:10.1016/j.rse.2004.02.007.

Woodward, F. I., and T. M. Smith (1994), Global photosynthesis and stomatal conductance: Modelling the controls by soil and climate, *Adv. Bot. Res.*, *20*, 1–41, doi:10.1016/S0065-2296(08)60214-1.

Woodward, F. I., T. M. Smith, and W. R. Emanuel (1995), A global land primary productivity and phytogeography model, *Global Biogeochem. Cycles*, *9*, 471–490, doi:10.1029/95GB02432.

Zhang, K., J. S. Kimball, M. Zhao, W. C. Oechel, J. Casano, and S. W. Running (2007), Sensitivity of pan-Arctic terrestrial net primary productivity simulations to daily surface meteorology from NCEP-NCAR and ERA-40 reanalyses, *J. Geophys. Res.*, *112*, G01011, doi:10.1029/2006JG000249.

Zhang, Y. Q., F. H. S. Chiew, L. Zhang, R. Leuning, and H. A. Cleugh (2008), Estimating catchment evaporation and runoff using MODIS leaf area index and the Penman-Monteith equation, *Water Resour. Res., 44,* W10420, doi:10.1029/2007WR006563.

Zhao, M., F. A. Heinsch, R. Nemani, and S. W. Running (2005), Improvements of the MODIS terrestrial gross and net primary production global data set, *Remote Sens. Environ., 95,* 164–176, doi:10.1016/j.rse.2004.12.011.

Zhao, M., S. W. Running, and R. R. Nemani (2006), Sensitivity of Moderate Resolution Imaging Spectroradiometer (MODIS) terrestrial primary production to the accuracy of meteorological reanalyses, *J. Geophys. Res., 111,* G01002, doi:10.1029/2004JG000004.

L. A. Jones, Q. Mu, and S. W. Running, Numerical Terradynamic Simulation Group, College of Forestry and Conservation, University of Montana, 32 Campus Drive, Missoula, MT 59812, USA.

J. S. Kimball, Flathead Lake Biological Station, 32125 Bio Station Lane, Polson, MT 59860-6815, USA.

K. C. McDonald, NASA Jet Propulsion Laboratory, 4800 Oak Grove Drive, Pasadena, CA 91109, USA.